Department of Precision and Microsystems Engineering

Measurement of Low Contact Angle Droplet Topography Using Optical Interferometry

Alok Bharadwaj

Report no	:	2019.034
Supervisor	:	Dr. Murali Ghatkesar
Co-supervisor	:	Dr. Lennino Cacace
Chair	:	Dr. Ir. Marcel Tichem
Specialization	:	Optomechatronics
Type of report	:	Master's Thesis
Date	:	26 September 2019

TU Delft
Delft University of Technology

Measurement of Low Contact Angle Droplet Topography Using Optical Interferometry

by

A. Bharadwaj

to obtain the degree of Master of Science
at the Delft University of Technology,
defended publicly on Thursday September 26, 2019 at 15:00 h.

Student number:	4744535	
Project duration:	October 10, 2018 – September 1, 2019	
Supervisor:	Dr. Murali Ghatkesar,	3ME, TU Delft
Co-supervisor:	Dr. Lennino Cacace,	3ME, TU Delft
	Ir. Eleonoor Verlinden,	3ME, TU Delft
Thesis committee:	Dr. Marcel Tichem,	3ME, TU Delft
	Dr. Gerard Verbiest,	3ME, TU Delft
	Dr. Arjen Jakobi,	TNW, TU Delft

This thesis is confidential and cannot be made public until December 31, 2020.

Abstract

Production and manipulation of microdroplets is an active are of research. The demand for finding new ways to produce microdroplets has resulted in a challenge to characterize these droplets. The problem becomes especially difficult for microdroplets which are placed on a transparent hydrophilic substrate. Ink-jet printing, Digital microfluidics, DNA synthesis are some of the applications which need topography measurements of low contact angle microdroplets. One application which is of interest is the sample preparation for Cryo Electron Microscopy (cryo-EM).

A recent development in the search for efficient sample preparation for cryo-EM is to use hollow microcantilevers (HMC). HMCs can isolate even a single sub-cellular component and help prepare samples confined in a femtoliter droplet. These droplets are dispensed on a hydrophilic Electron Microscopy grid (EM-grid). By controlling the thickness of the water layer on the EM-grid through evaporation, it is possible to make the HMC technology more reliable by reducing sample wastage. However, such a control loop is absent. A real-time topography measurement of such droplets can serve as a control signal which can be used as feedback for a control loop.

The objective of this project is to investigate the feasibility of optical methods to measure the topography information of a low contact angle microdroplet. The scope of this project is limited to develop a tool for a droplet which is supported by a glass slide (droplet-on-glass). In a subsequent study, the tool will be tested for droplets supported on grid (droplet-on-grid).

An optical interferometry setup is proposed as a solution. A Mach-Zehnder interferometer is built to obtain the experimental fringes. A Single Frame Fourier Transform technique was used to analyze the data and obtain the results. Droplets of glycerol were dispensed on a glow discharged glass slide. Topography of the droplet was obtained until complete evaporation and a detection limit of 165nm was achieved. The accuracy of the method was found by comparing the results obtained with a Bruker White Light Interferometer (Bruker-WLI) in Phase Shifting Interferometry mode. An accuracy of 23% was observed. The proposed setup had a repeatability of 14.7nm. To measure the reproducibility of the setup, a 3d printed structure which had the same size and shape as that of a droplet was used. The reproducibility of the setup was found to be 19.8nm over three days.

Simulations were performed to analyze the effect of filter shape, filter width and the carrier frequency. Based on these findings, steps to measure a droplet-on-grid system with the proposed setup is explained.

Further, to test the capabilities of the instrument the evaporation of a large water droplet on a EM-grid was observed using the proposed setup. It was found that the motion of fringe pattern as the droplet evaporates could give a good indication to control the evaporation time of even conventional machines, which do not employ hollow microcantilevers to dispense small droplets. However, final validation of the proposed setup with the cryo-EM is yet to be performed due to time constraints.

As a recommendation for future work, new ways of dispensing samples on the EM-grid are explored. The necessary steps required to validate the setup with a cryo-EM are explained. Further, some ways in which the analysis time could be reduced are explored. This will be helpful in developing a software necessary to implement a real-time solution.

A. Bharadwaj
Delft, September 2019

List of Figures

List of Tables

Contents

1

Introduction

Nature has found useful ways to manipulate liquid droplets. Leaves of plants like Colocasia which are commonly found in South and South-East Asia have developed microscopic texture which repel water. This has a survival advantage; pathogens such as mold and fungi normally grow in moist places. If water were to wet the leaves of Colocasia, it would be susceptible to attack by these pathogens. But instead, water simply forms a small bead structure and rolls down, keeping the leaves dry. Figure 1.1 shows the image of beads forming on the surface of a Colocasia plant leaf.

Figure 1.1: Water droplet forming a bead on the leaves of a Colocasia plant [1]

Physical phenomena involving water droplets have captured the attention of scientists for well over a hundred years. Even today producing and manipulating liquid droplets are an active field of research. This is due to the many applications it has. Digital microfluidics manipulates individual droplets for lab-on-chip applications [2]. Advances in nanofabrication techniques have made it possible to produce and manipulate liquids droplets which have sub-picoliters volume. Production and manipulation of such microdroplets is responsible for the development of high resolution ink-jet printing [3], protein synthesis [4] etc. At TU Delft, development of hollow microcantilevers (HMC) to aspirate and dispense microdroplets has increased the interest in developing an efficient sample preparation setup for Cryo-Electron Microscopy.

Cryo-Electron Microscopy (cryo-EM) is a type of electron microscopy which can image samples at cryogenic temperatures. It is possible to image biological molecules such as proteins and DNA at near atomic resolution using this method. Improving sample preparation for cryo-EM has attracted the attention of scientists in recent years [5, 6]. One such advanced sample preparation technique involves dispensing liquid droplets having volumes in the range of femtoliters to picoliters using a hollow microcantilever (HMC) [7]. This makes it possible to isolate a single bio-molecule from its environment by aspirating a small amount of liquid which contains the bio-molecule. This liquid can then be dispensed on an Electron Microscope grid (EM-grid) and be imaged using a cryo-EM

An introduction to the technique of using HMC for cryo-EM sample preparation is given in the next section. Following that, the issue of controlling evaporation time which has impeded the growth of this technique is explained. Integrating the HMC setup with a device to measure the topography of droplets is proposed as a solution. A summary of literature review is given to list some commonly used measurement techniques to obtain topography information. Finally, an argument for using optical interferometry as a possible measurement technique is made and an approach to demonstrate the effectiveness of this method is laid out.

1.1. Hollow Microcantilevers for cryo-EM

A hollow microcantilever (HMC) is a special type of microcantilever, which has a hollow channel along its axis. The hollow channel connects a liquid reservoir to an aperture. It has been demonstrated that such a device could be used to dispense liquids having volumes in the range femtoliters to picoliters [7]. By modifying this setup, it is also possible to aspirate liquids from a solution. This is the principle used to produce samples for cryo-EM.

A bath containing the biological specimen of interest is bought under an inverted microscope. The HMC setup is used to aspirate a sub-cellular size biological specimen. It is then dispensed on an EM-grid. The EM-grid is then taken to a plunging mechanism where it is plunge frozen into a liquid ethane bath. The whole setup is inside a humidity chamber maintained at 75% humidity.

An EM-grid consists of a metallic mesh with circular or square holes. The size of the holes are measured in terms of number of holes per inch, called mesh size. A thin film of carbon is present on top of the grid. Holes are present on the carbon film. Figure 1.2 shows the structure of an EM-grid.

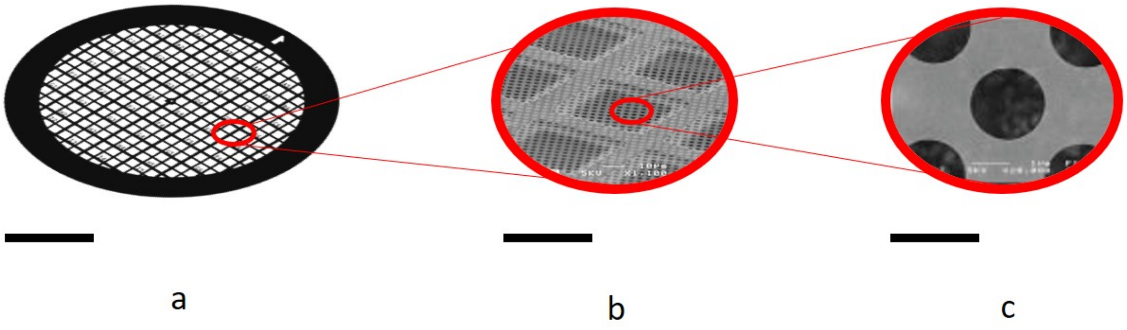

Figure 1.2: Structure of an EM-grid (a) Full view of an EM-grid, scale bar 1 mm [8], (b) Closer observation of the grid, scale bar 100 microns [9], (c) Measurement of holes in the carbon layer, scale bar 1 micron [9]

The sample is dispensed from the HMC on the carbon film. If the grid surface is hydrophobic, the liquid bulges at the center and the center thickness becomes too high. This causes problem at later stages in using the cryo-EM. To make the surface more hydrophilic the grid is subject to glow discharge, typically using oxygen plasma. The contact angle of liquid after glow discharge would be less than 20 degrees. To prevent droplets from getting stuck to the cantilevers, a hydrophobic coating is applied to the cantilever surface.

The dispensing of liquid on the EM-grid can be broken down into following steps.

1. Cantilever approach the EM-grid

2. A pressure pulse of 4 bar is applied for 12 sec
3. Cantilever is withdrawn after dispensing

Figure 1.3 illustrates the sequence of steps mentioned above.

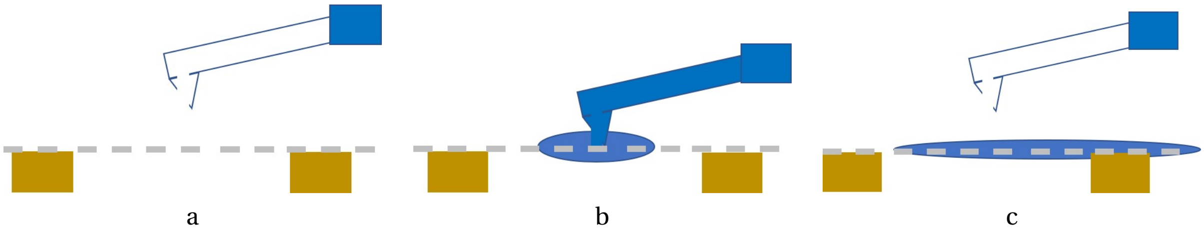

Figure 1.3: Dispensing droplets using HMC on EM-grid

1.1.1. Controlling evaporation time

In practice several challenges need to be overcome for this method to be reliable. One problem facing scientists using this setup is the inability to determine the exact moment when plunging mechanism needs to get activated. Currently the plunging mechanism is activated after waiting for an arbitrary moment of time. During this period, certain amount of liquid is lost to evaporation. A precise control of this evaporation time is necessary for the following reason.

Evaporation time determines the amount of liquid left behind on the EM-grid, thus affecting the thickness of the water layer. After plunging the droplet becomes vitrified. The resulting ice layer thickness has significant effect on the contrast obtained in the final cryo EM image. It is necessary to optimise the evaporation time to ensure the right amount of ice layer thickness is obtained.

Cryo-EM imaging is typically done using phase contrast method [10]. In phase contrast imaging, the unscattered electrons and single elastic scattered electrons contribute to the signal information. Scattering takes place due to the collision of electrons with water molecules. An elastic collision does not lead to energy loss, while an inelastic collision transfers energy to the specimen leading to damage. Multiple elastic scattering contributes to the noise of the image. The probability of inelastic collision and multiple elastic collisions increase with the ice layer thickness. These effects can be significant when the ice layer thickness is larger than the mean free path of the electrons. The inelastic mean free path of electrons at an operating voltage of 120kV is about 203nm [11]. It is required to ensure that the ice layer thickness is less than this critical value during the sample preparation step itself.

Using the HMC setup, it is possible to control the ice layer thickness by adjusting the evaporation time. However, to do that it is first necessary to monitor the thickness of the water layer in real time, as it evaporates. Once such a system is in place, it can be used as a signal to the plunging mechanism. Once a desired thickness value is obtained, the plunging mechanism can be activated. This ensures that the ice layer has a suitable thickness for cryo imaging.

1.1.2. Measurement of droplet topography

A topography information of the droplet gives the value of the water layer thickness at every point in a frame. It is possible for the user to select any locations to monitor the height in real time. The measurements at these points can be used to monitor the evaporation time of the droplet. Once the measurements cross a certain threshold value, it can be used to send control signal for the plunging mechanism to start vitrification.

As a first step, some of the challenges were addressed by taking reasonable simplifications. These are highlighted in the following section.

1.2. Challenges

Any measurement system that would be proposed should be validated by a standard calibrated instrument. This is done by measuring the same object once using the proposed setup and again with the standard setup. Since the object under consideration is a fast evaporating droplet, the evaporation losses need to be mitigated. Water droplets is generally used for cryo-EM applications using hollow microcantilevers. However, at normal laboratory conditions the evaporation time of femtoliter water droplets is few seconds thus evaporation becomes a limiting factor. To mitigate this issue, droplet of glycerol are used for validation purposes. The vapour pressure of glycerol is less than 1 mmHg [12]. This is ten thousand times smaller compared to water, therefore evaporates much slowly. It was found by experiments that a glycerol droplet with an initial radius of 50 microns and a height of 2 microns takes about 6 hours to evaporate completely. This gives enough time for measurement and validation.

The use of an EM-grid as a supporting structure to carry the droplet also poses another significant challenge. This is mainly due to the fact it becomes harder to transfer the grid between setup for validation. The EM-grid is very fragile and is prone to damage by frequent handling. This further limits the type of instruments that can take the EM-grid as an input. A possible solution to this problem is to use cryo-EM instrument for validation purposes. However, this would be impractical. This is because in the beginning, there would be lot of repeated measurements and many failed samples. The waiting time to use cryo-EM for each of those experiments would limit the progress that could be made.

A two step approach is proposed to solve this problem. In the first phase, a simpler model is chosen which doesn't use grid as a supporting structure. A smooth and transparent solid surface, such as glass, can be used instead. This is called a droplet-on-glass model. Measurements for this model can be easily validated using several optical equipment which are easily accessible. Once the proposed setup is validated against this standard equipment, the same setup could be used with an EM-grid as the support structure, which is called the droplet-on-grid model. Since the setup is calibrated in the beginning, the number of repeated measurements would be lower. Thus the dependency on cryo-EM would be greatly reduced in the second step.

The choice of the measurement technique should be made based on several criteria. Detection limit and adaptability for EM-grid forms two primary factors which influence this choice.

1. *Detection Limit:* Detection limit is defined in terms of the smallest height that can be detected by an instrument. Since the critical ice layer thickness for cryo-EM imaging is about 200 nm, the detection limit should be less than this.

2. *Adaptability:* Adaptability for EM-grid criteria is generally by the ease with which the same setup be adapted for a droplet-on-grid model. The major requirement here is space. If there is enough space to place a plunging mechanism, and a liquid nitrogen bath then the setup can be suited for EM-grid. Another obvious requirement which needs to be met is that the measurement principle should not bar the use of a EM-grid support structure. There would be many measurement principles which can be used for the droplet-on-glass model, but only a subset of these could also be used for droplet-on-grid model.

Since sessile droplets are studied in literature for a long time, it is possible to find suitable technique which can also be adapted for the case of EM-grid. The studies generally do not report the detection limit of their used setup. In that case, calculations were made based on the smallest data point reported using the geometry of a sessile droplet. The following section summarises the main measurement techniques which are studied in literature.

1.3. Literature Review

The popular measurement techniques used to investigate the evaporation of sessile droplets are broadly classified as follows:

1.3.1. Visual Technique

Visual techniques makes use of an optical microscope to extract the profile of a droplet. This is generally accomplished by recording the side view of a droplet as it evaporates. The profile view can give information about droplet height, contact radius and contact angle with good degree of certainty. An optical goniometer is a standard instrument used for measuring contact angle and is a standard technique.

There are some modifications that could be done, for instance by adding fluorescent particles to add contrast to the surface. Hu et. al. [13] used such fluorescent particles of 0.75 micron diameter to find the surface profile of droplets. The decrease in volume with time is shown in the Figure 1.4. The volume corresponding to the smallest data point reported is about 30 nL. For a circular contact radius of 0.85mm, this volume corresponds to a height of 40 microns. Rowan et al. [14] used a reflection technique with visual microscopy to monitor droplets having initial volumes of 50 nL and 80 degree contact angle. This method is also applied by Picknett et. al. [15] and Butt [16] to measure droplets having initial volumes in picoliter to microliter range.

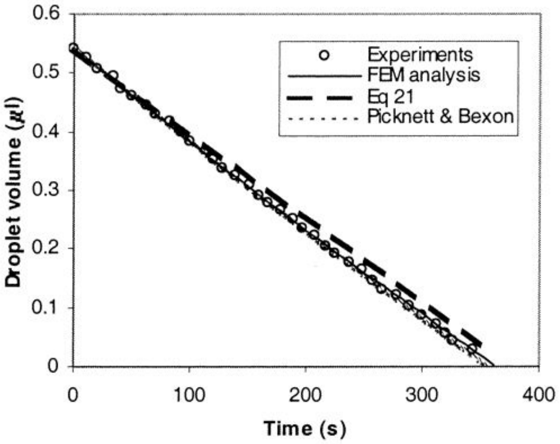

Figure 1.4: Volume of the droplet as a function of time. The smallest data point has a volume 30 nL [13]

A limitation of visual microscopy is the resolution limit of optical microscopes. However, this has an advantage of being simple, thus can be adapted for droplet-on-grid model by attaching a camera. This solution has been implemented and published in literature [6]. The device, Spotiton, has an ink-jet printer which can dispense droplets on grid and can observe the droplets from a camera attached to its side. Figure 1.5 shows the images taken from this camera. However, it is hard to extract the surface profile of droplets which have very low contact angle (less than 15 degree) due to the resolution limit.

1.3.2. Mechanical Technique

One of the recent advances in monitoring microdroplet evaporation behaviour is to study the change in mass by making use of dynamic behaviour of resonators. Cantilevers are generally used for this purpose. For case of a large contact angle droplet, the cantilever bends in relation to the contact angle, and thus static deflection can be used to measure the contact angle. Using mass and contact angle information, it is possible to derive all other geometric properties.

Golovko [17] used this method to monitor the evaporation of a droplet having 10 picoliters initial volume and 90 degree contact angle, using a hydrophobized AFM cantilever surface. Arcamone et. al [18] used NADIS dispensing technique to produce droplets having volumes in the range attoliter to femtoliter and monitored evaporation using a nanomechanical mass sensor. The droplet had an initial contact angle of 60 degree and the height of the smallest droplet reported was 2 microns. The detection limit of this device was reported as 100 femtograms. Figure 1.6 shows the mass result obtained using this device for different initial mass.

Mate et al. [19] used AFM dipping technique to measure the thickness of a thin film of polymeric liquid on a glass substrate. The technique could be, in principle, modified to measure the droplet surface profile.

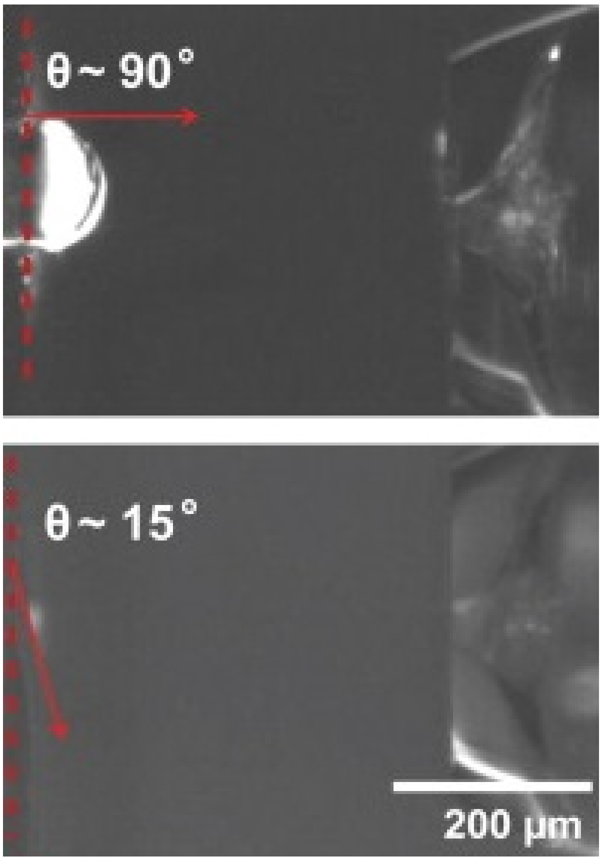

Figure 1.5: Image of a droplet placed on a hydrophobic EM-grid (top) and a hydrophilic EM-grid (bottom) in the Spotiton setup [6]. The dashed red line indicate the EM-grid surface

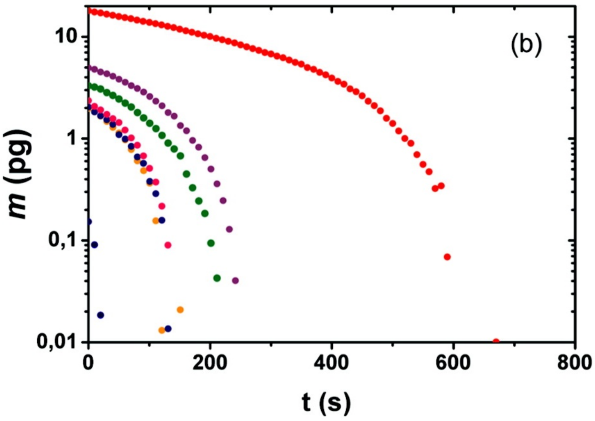

Figure 1.6: Mass of droplet as a function of time with different initial masses [18]

Mechanical techniques using resonant modes of cantilevers can provide precise measurements of mass for the type of droplets considered in this report. However, these techniques are mainly a contact type measurements and they need to be physically in contact with the EM-grid or the sample, which increases risk of contamination.

1.3.3. Optical Technique

These techniques make use of optical phenomena such as interference, holography to obtain a three-dimensional surface profile of an evaporating droplet. A main advantage of this technique is the ability to perform remote monitoring of droplets placed on EM-grid, as it eliminates the risk of contamination. Optical techniques are also fast, and robust techniques making it an attractive choice for the present purpose.

Sun et al. [20] used a Dual Channel Simultaneous Phase Shifting Interferometry (DCSPSI) to capture two interferograms with a known phase shift of $\pi/2$. Such a technique could be used to obtain topography in real time. Figure 1.7 shows the surface profiles for an evaporating water droplet. Instantaneous mass of the droplet was calculated from the surface profile. The smallest mass recorded using this method is 2.9 ng.

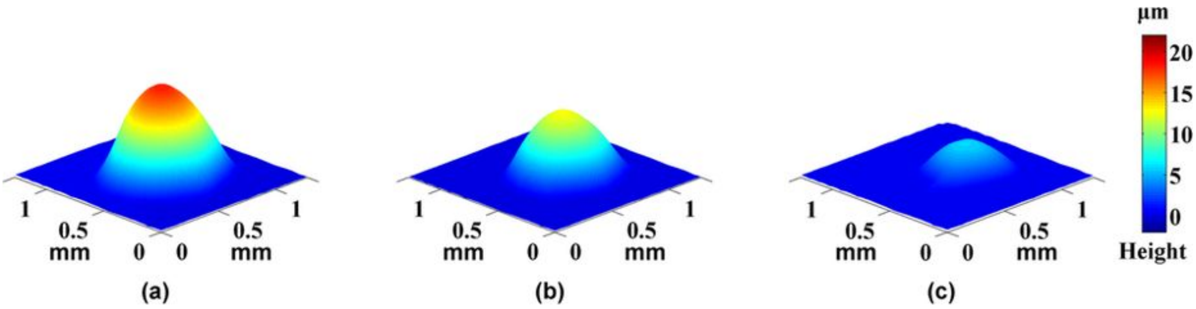

Figure 1.7: Three dimensional surface profile recorded for an evaporating water droplet using DCSPSI [20]

Spatial phase shifting usually requires two or more CCD cameras to capture interferograms. However there are algorithms to extract phase from an interference pattern using only one interference pattern. The most popular single frame algorithm is using the Fourier transform method [21]. Spatial phase shifting interferometry using single frame was shown to provide phase measurements for droplets and cells by Huang et al. [22]. The initial height of the droplet was less than 10 micron, but the system was capable of measuring sub-micron heights. The Fourier Transform method uses a spatial carrier to extract the phase signal from the interference pattern. This method works best when the phase jumps between two pixels do not cross 2π. For low contact angle droplets, the phase jump between two pixels is much less than 2π and hence are suitable.

1.4. Selection

Visual techniques using a camera has a main advantage of being simple. However, it cannot satisfy the detection limit criteria as it cannot resolve height below the resolution limit. Measurements using mass sensing can provide excellent resolution and has very low detection limit. However unless a major change is made to the grid holder, it is very difficult to use this method for measurements on EM-grid.

Optical techniques are therefore much more favourable as a concept choice. Further, interferometry has been demonstrated to give a topographical information of a droplet as it evaporates. Therefore, optical interferometry is the best choice to measure the topography of a droplet.

There is still several ways of implementing interferometry. This requires testing several different setup and making a choice based on the experience of building those setup.

1.5. Research Question

What is the detection limit of a topography measurement device which uses optical interferometry to measure very low contact angle liquid droplet?

1.6. Approach

To accomplish the stated research objectives, the following tasks were executed planned

1. Evaluate different principles using first principles approach
2. Simulation of the selected technique to verify the data analysis
3. Test different implementation strategies for optical interferometry

4. Experimental evaluation of the selected strategy
    (a) Measurement for a simple case of a sessile droplet on glass
    (b) Verification using a standard instrument
    (c) Measurement for the case of a droplet on grid
    (d) Verification using cryo-EM
5. Miniaturisation using optical design strategies

Due to constraints of time, all the tasks up to 4(c) were executed. Verification of results using cryo-EM and miniaturisation using optical design are proposed as recommendations for future work.

2

Measurement of Low Contact Angle Droplet Topography using Optical Interferometry

Abstract
The interest in studying new ways of producing and manipulating liquid microdroplets has created a need to find new ways to characterise these droplets. Measuring low contact angle droplets is important for various applications such as protein synthesis, digital microfluidics and sample preparation for Cryo Electron Microscopy. In this report, the effectiveness of optical interferometry to measure the topography of low contact angle microdroplets is studied. A Mach-Zehnder interferometer was built to obtain interference fringes. Interference fringe patttern was analysed using a Single Frame Fourier Transform technique. Experiments were done by dispensing glycerol microdroplets on a hydrophilic glass surface. The measurements were validated using Bruker White Light Interferometer. The setup had an accuracy of 23% and repeatability of 14.7nm. The detection limit of the device was 165nm. The reproducibility of the setup was found to be 19.8nm over three days. Using this setup it was possible to measure the evaporation dynamics of the glycerol droplet.

Keywords: Low contact angle droplets, microdroplet, Fourier Transform interferometry, droplet topography, droplet evaporation

2.1. Introduction

There has been a steady rise in the interest to study the phenomena associated with small scale liquid droplets. This trend is driven by the need to produce and manipulate liquid droplets in a variety of situations. Production of microdroplet, those with diameters typically less than hundred microns, has immense potential for digital microfluidics [23]. Ink-jet printing of femtoliter droplets is used to create organic transistors [3], better drug dispensing techniques [24], tin soldering for electronic manufacture [25] etc. Each of these fields demand the ability to produce and manipulate liquid droplets which have sub-picoliters volumes.

The progress towards building tools to produce microdroplets has given raise to a new problem of characterising such droplets. For a droplet placed on a solid surface, the contact angle becomes an important variable which needs to be measured. The contact angle characterises the nature of interaction between the droplet and the solid surface. The most popular tool of measuring the contact angle is a goniometer. This instrument uses a high resolution camera and microscope to observe the droplet surface profile from its side. However using an optical microscope is limited by the resolution limit of such devices. Therefore it becomes challenging to observe droplets with extremely low volumes, and low contact angles.

It has been shown by previous studies that optical interferometry could be used to obtain the topography of liquid droplets having low contact angles [20, 22]. This information would be very useful to study the dynamics of such droplets. The principle of optical interferometry is to find the relative phase difference between a beam of light passing through the sample and a reference beam. This is achieved using the interference of light, by capturing interference fringes on a CCD. There are several implementation strategies to obtain interference fringe and to analyse the data.

One of the most common ways of extracting phase from interference signals is to use phase shifting interferometry [26]. Temporal phase shifting interferometry (TPSI) is a method of analysing fringes using phase stepping with two or more frames. Two or more interference fringe pattern are recorded with a known phase shift between them. However, TPSI cannot be used for recording dynamic processes such as evaporation of droplets. Spatial phase shifting interferometry can overcome this limitation by spatially separating the different interference patterns. This can be achieved by projecting interference fringes with different phase shifts on separate areas of a single CCD [27], or by projecting on to multiple CCDs all of which can record the interference pattern simultaneously [20]. There are several algorithms which can be used corresponding to the number of interferograms captured. Sun et al. [20] used two CCDs to capture interference fringes which had a phase shift of $\pi/2$ to obtain droplet topography for a water droplet placed on glass.

Analysing interference fringe pattern from a single frame is a much simpler implementation strategy due to lesser number of components involved. Fourier transform method [21] is the most popular technique to extract phase field this way. It makes use of a carrier signal for phase modulation. Using proper filters it is possible to extract the phase using fast algorithms. A combination of Fourier transform and spatial phase shifting interferometry was used to study the evaporation of water droplets and apoptosis of Jurkat cells [22]. Hilbert Phase Microscopy, which uses Hilbert transform on a fringe pattern to obtain the phase field was used to get the height map of a set of blood cells [28].

This study is aimed at understanding the effectiveness of Single Frame Fourier Transform technique to measure the topography of a droplet placed on a smooth and transparent glass surface. Further, the feasibility of this technique to measure droplet topography for droplets placed on non-ideal substrates is also considered. One such non-ideal substrate is an Electron Microscopy grid (EM-grid).

In the following section, the principles behind the Single Frame Fourier Transform technique is explained in detail. The sample preparation method, details of the proposed setup and validation method are explained after that. Results obtained from the evaporation of a glycerol droplet suggest the proposed method has a detection limit of 165 nm, and an accuracy of 23%. Further the repeatability of the proposed setup was found to be 14.7nm and it had a reproducibility of 19.8 nm over three days.

2.2. Principle

An interference fringe pattern is the intensity distribution recorded by the CCD detector. Figure 2.3 shows a typical example of an interference fringe pattern.

This can be formulated mathematically as follows:

$$i(x, y) = a(x, y) + b(x, y) \cdot cos\left(\Delta\phi(x, y)\right) \tag{2.1}$$

Here, $i(x, y)$ represents the interference pattern as an intensity distribution over the CCD. It is represented as a function of x and y which is the distance of a pixel from the origin as defined in the Figure 2.3. For a pixel in the j'th column and i'th row, starting from the origin

$$x = j \cdot \delta$$
$$y = i \cdot \delta$$

Where δ is the size of a single pixel.

$a(x, y)$ and $b(x, y)$ represent the DC component and modulation amplitude of the interference pattern. The term $\Delta\phi(x, y)$ is the Optical Phase Difference (OPD). The OPD is the resultant phase field obtained by adding the signal, $\phi_s(x, y)$ and carrier waves $\phi_c(x, y)$. The signal wave contains the desired height information, $h(x,y)$.

$$\begin{aligned}\Delta\phi(x,y) &= \phi_s(x,y)+\phi_c(x,y)\\ \phi_s(x,y) &= \frac{h(x,y)\cdot(2\pi(n-1))}{\lambda}\\ \phi_c(x,y) &= 2\pi f_x\cdot x+2\pi f_y\cdot y\end{aligned}$$

Where n is the refractive index of the test sample (droplet) and λ is the wavelength of the light used. The carrier wave is characterised by the carrier frequencies f_x and f_y in x and y directions respectively. These are spatial frequency which is related to the fringe spacing as

$$\begin{aligned}f_x &= \frac{1}{\Delta x\cdot\delta}\\ f_y &= \frac{1}{\Delta y\cdot\delta}\end{aligned}$$

Δx and Δy are the fringe spacing, in pixels, observed in the interference fringe pattern. The carrier frequencies, therefore has the units m^{-1} in SI standards.

Equation 2.1 can be expressed in complex notation as follows

$$i(x,y)=a(x,y)+\frac{1}{2}\cdot b(x,y)\cdot(e^{-i\Delta\phi(x,y)}+e^{i\Delta\phi(x,y)}) \tag{2.2}$$

Which can be simplified as

$$i(x,y)=a(x,y)+\left(0.5\cdot b(x,y)\cdot e^{-i\phi_s(x,y)}\right)\cdot e^{-i\phi_c(x,y)}+\left(0.5\cdot b(x,y)\cdot e^{i\phi_s(x,y)}\right)\cdot e^{i\phi_c(x,y)}$$

$$i(x,y)=a(x,y)+c(x,y)\cdot e^{-i\phi_c(x,y))}+c^*(x,y)\cdot e^{i\phi_c(x,y)} \tag{2.3}$$

where

$$c(x,y)=\left(0.5\cdot b(x,y)\cdot e^{-i\phi_s(x,y)}\right) \tag{2.4}$$

and * denotes complex conjugates.

Taking the Fourier Transform of Equation 2.3 we get,

$$I(u,v)=A(u,v)+C(u-f_x,v-f_y)+C^*(u+f_x,v+f_y) \tag{2.5}$$

Where u and v are the coordinates in frequency space. Equation 2.5 represents three distinct peaks in the Fourier space. This is because, the terms $a(x,y)$, $b(x,y)$ and $c(x,y)$ are all slowly varying compared to the carrier frequency. The three peaks are centered at locations $(-f_x,-f_y)$, $(0,0)$ and (f_x,f_y). Figure 2.1 shows the amplitude of a normalised Fourier transform of Figure 2.3. The interference fringe pattern from Figure 2.3 has a carrier frequency of $8mm^{-1}$ in both x and y directions. Therefore, the two side peaks appear at the location of carrier frequency.

Multiplying the $I(u,v)$ with a filter to extract only one peak, we get

$$C(u-f_x,v-f_y)=I(u,v)\cdot F(u,v)$$

Tranlating this peak to the center by shifting the image by an amount f_x and f_y in x and y directions, we get $C(u,v)$. $C(u,v)$ is equal to the Fourier transform of the Equation 2.4. Therefore taking the inverse Fourier transform we get

$$c(x,y)=F^{-1}(C(u,v)) \tag{2.6}$$

which is a complex number. The real part and the imaginary part of this can be used to demodulate the phase using

$$\phi_w(x,y) = tan^{-1}\left(\frac{imag[c(x,y]}{real[c(x,y)]}\right) \tag{2.7}$$

The term $\phi_w(x,y)$ is wrapped between $-\pi/2$ to $\pi/2$. Thus, it needs to be unwrapped using a suitable algorithm. Once it is unwrapped, the signal phase field $\phi_s(x,y)$ is obtained. The height profile can be obtained using the formula

$$h(x,y) = \frac{\phi_s(x,y)\cdot\lambda}{2\pi(n-1)} \tag{2.8}$$

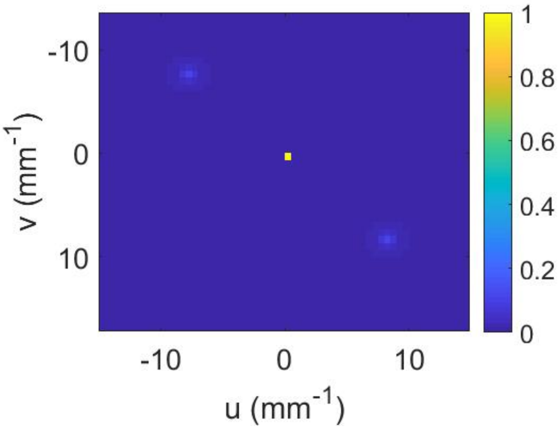

Figure 2.1: Central and side peaks observed for a simulated interference fringe having carrier frequency $8mm^{-1}$

In the supplementary information 5.1, the procedue of SFFT is illustrated for a 1D interference fringe pattern. The SFFT algorithm is dependant on three parameters: filter shape, filter width and carrier frequency. The effect of these parameters are presented in supplementary information 5.2. Further, the phase unwrapping algorithm plays a crucial part in the result obtained by the SFFT algorithm. Two phase unwrapping techniques have been considered and they are explained in supplementary information 5.3.

2.3. Materials and Methods

2.3.1. Simulations

The geometry of a droplet is that of a spherical cap as shown in Figure 2.2. For a spherical cap, atleast two variables need to be given as an input to constrain the whole model. The rest can be calculated using geometric relations.

The reference height maps were generated for a contact radius of 50 microns. The height of the droplet was varied to obtain different reference height maps. The height map was generated considering a droplet placed at the center of the image. The spherical cap geometry in two dimensions can be obtained using the following relation

$$h(x,y) = \begin{cases} 0 & (x-x_0)^2+(y-y_0)^2 > R^2 \\ h_0 - R + \sqrt{R^2-(x-x_0)^2-(y-y_0)^2} & \text{otherwise} \end{cases} \tag{2.9}$$

h_0 is the droplet height, R is the spherical radius of the droplet and (x_0, y_0) is location of the center of the droplet. By using different values for h_0, different droplet surfaces can be modelled. The reference droplet height can be used to obtain the phase field as .

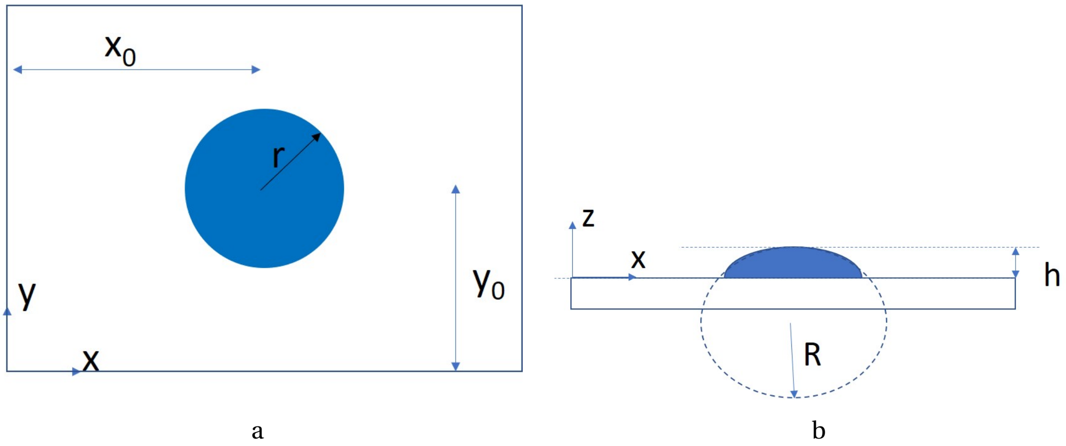

Figure 2.2: Schematic of a sessile droplet (a) viewed from the top and (b) viewed from the side

$$\Delta\phi(x,y) = k\cdot\big(h(x,y)\cdot(n-1)+\phi_c(x,y)\big)$$
$$k=\frac{2\pi}{\lambda}$$

Where $\Delta\phi(x,y)$ is the phase difference between reference and test arms of an interferometer, n is the refractive index of the droplet and λ is the wavelength of light used. The carrier signal can be modelled using $\phi_c(x,y)$ using equations mentioned earlier.

A noise signal $g(x,y)$ is added to $\Delta\phi(x,y)$ before obtaining the interference pattern. The noise used here is normally distributed with a mean at zero and a standard deviation σ. For the analysis the standard deviation is set constant as 0.5 rad.

$$\Delta\phi_n(x,y) = \Delta\phi(x,y)+\sigma\cdot g(x,y)$$

The noisy phase field is then used to obtain the interference pattern as

$$i(x,y) = a(x,y)+b(x,y)\cdot cos(\Delta\phi_n(x,y))$$

The terms $a(x,y)$ and $b(x,y)$ can be used to model the DC offset and the modulation amplitude respectively. Figure 2.3 (a) shows an example of a simulated interference fringe pattern using the method described here. Figure 2.3 (a) is obtained with no Gaussian noise added to the phase, while 2.3 (b) is simulated with a Gaussian noise with zero mean and 0.5 rad standard deviation.

2.3.2. Experimental Methods

Sample preparation

Small volumes of glycerol were dispensed on a clean, smooth glass plate using an AFM cantilever. The AFM cantilever was cleaned for two minutes in DI water and then in a solution of IPA. The bottom surface of the cantilever, which contacts the droplet, was sputter coated with gold for 3 minutes at 10mA current giving a thickness of 30nm. Figure 2.4 shows the surface of the cantilever before and after sputter coating.

A clean glass slide was chosen to dispense the glycerol droplets. A high quality diamond scribing pen (Manufactured by Ted Pella, product number 54468) was used to make scratch marks on the glass slide. The slide was then cleaned with DI water to remove any sharp cut pieces. It was also cleaned with IPA to remove any water layer remaining on the slide. The glass slide was then surface treated with oxygen plasma for 25

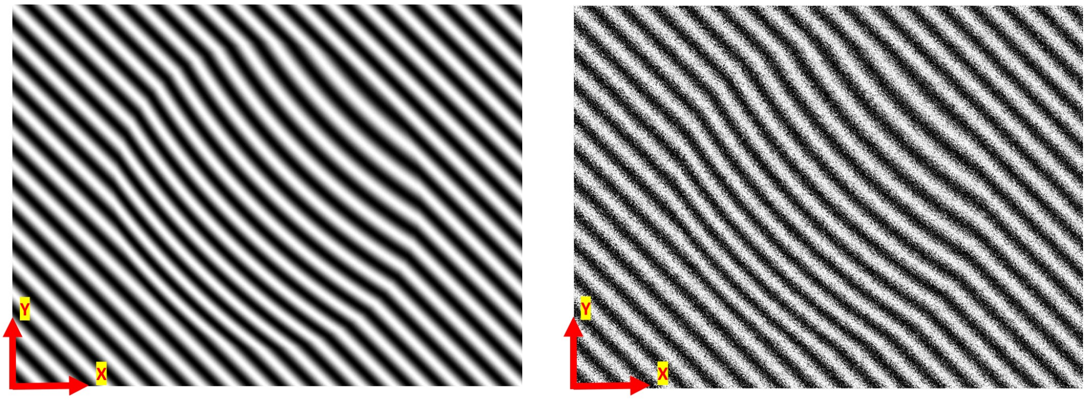

a b

Figure 2.3: A simulated interference fringe pattern (a) without adding Gaussian noise (b) after adding Gaussian noise of zero mean and 0.5 rad standard deviation

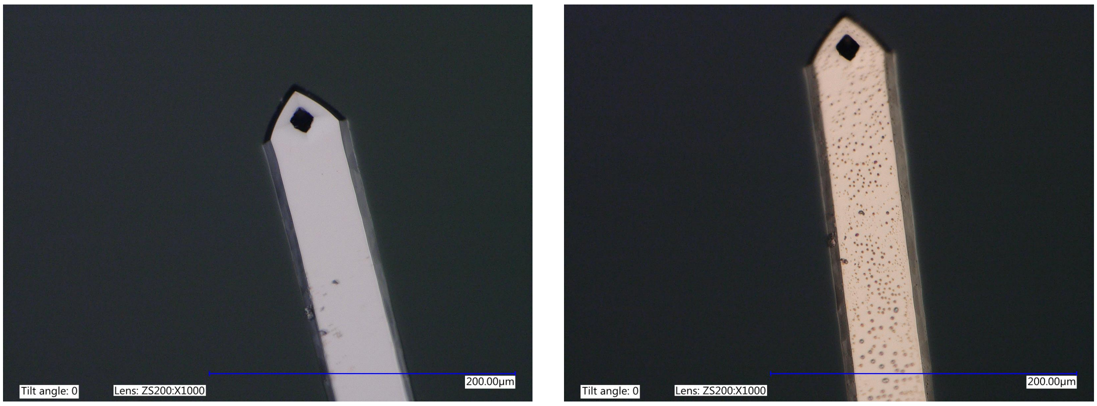

a b

Figure 2.4: AFM cantilever (a) before sputer coated with gold and (b) after sputter coating with 30nm gold layer

minutes to make the surface hydrophobic.

The coated AFM tip is first bought in contact with a large droplet of glycerol placed on another glass slide. It is then made to approach the plasma treated glass surface. Surface tension draws the liquid droplet from the tip into the glass plate. While withdrawing the tip, it is observed that the cantilever bends slightly due to the attraction between the tip and the glass surface. At some point it quickly snaps back. This snap action is found to affect the shape of the droplet. Instead of a circular shape, the droplet has a protrusion from one point. Figure 2.5 illustrates this step.

Mach-Zehnder Interferometer

Mach-Zehnder interferometer setup was built to obtain the interference fringes. The schematic of the setup and the photograph is shown in Figure 2.6.

A He-Ne laser (633 nm) was used as a coherent source of light. The intensity of the laser was controlled using a Neutral Density filter (ND-Filter). Incident light was split to form a reference arm and a test arm at the first beam splitter (BS1). Two 45-degree mirrors were used to combine the light from the two arms at the second beam splitter (BS2). The interference pattern was captured using a CCD camera which had a pixel resolution of 640 x 480. The pixel size of the camera used is 3.12 micron.

The prepared sample is introduced in the test arm. The imaging lens (L1) was used to magnify the droplet on the CCD detector. The focal length and magnification of the lens used was 60mm and 10x respectively. A

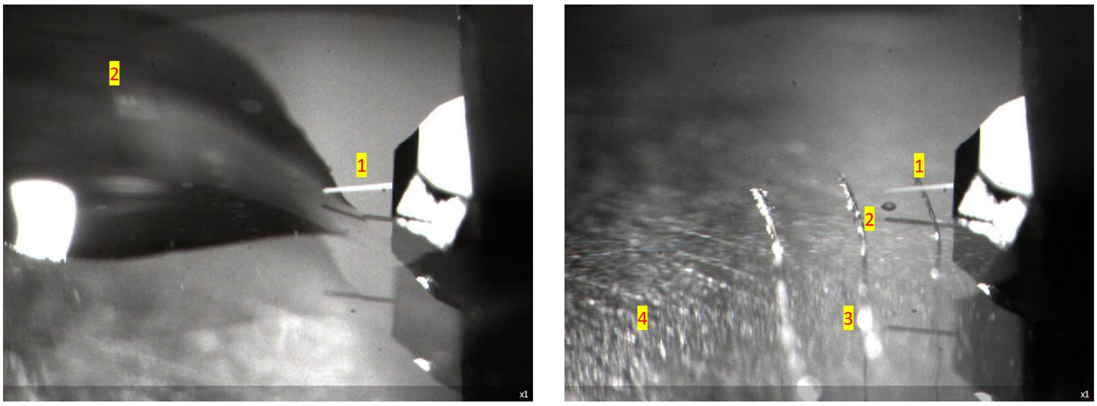

a

b

Figure 2.5: (a) AFM cantilever (1) approaching the edge of a large glycerol droplet (2) and (b) AFM cantilever (1) withdrawing after dispensing a glycerol droplet (2) near the scratch marks (3) made on the glow discharged glass slide (4)

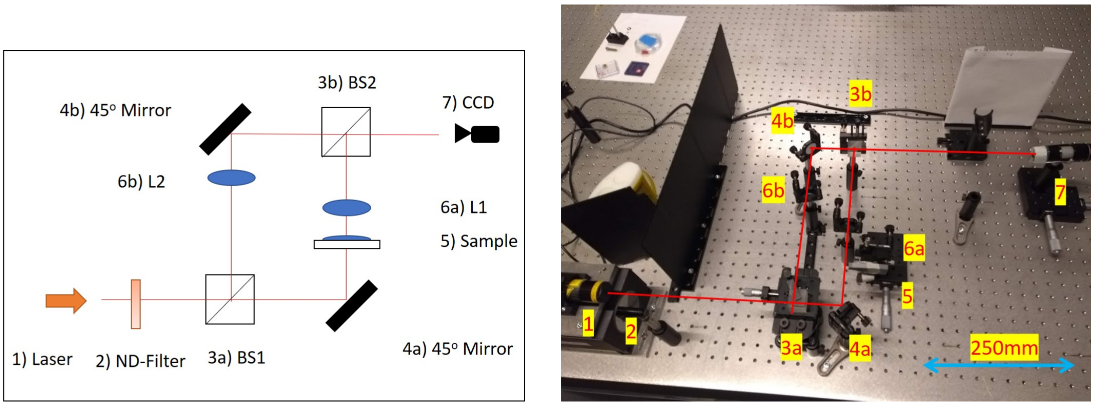

a

b

Figure 2.6: (a) Schematic of a Mach-Zehnder interferometer showing the components (1) Laser, (2) Neutral Density Filter (3a and 3b) Non-Polarised Beam Splitters, (4a and 4b) Mirrors, (5) Sample, (6a and 6b) Lens, and (7) CCD. (b) photograph of the setup

lens L2 was used on the reference arm for wavefront correction.

Carrier waves are generated in the interference pattern by introducing tilt in the optical setup. The second beam splitter BS2 was tilted in x and y direction. This affects the light going through the test arm and shifts the position of the corresponding laser spot on the detector. The 45-degree mirror in the reference arm was used to move the laser spot corresponding to the reference arm to obtain uniform illumination at the detector. The resulting interference pattern consists of parallel lines.

Experiments on Grid

A grid holder was designed using Envisiontec high resolution 3d printer. The grid holder was designed to accomodate a finder grid firmly in place and to mount it on the Mach-Zehnder interferometer setup. The Figure 2.8 shows the dimensions of the grid holder and the final 3d printed part.

Validation

To validate the proposed setup, it is required to compare the results obtained with a standard instrument. Bruker White Light Interferometer (Bruker-WLI) (Model num: Contour GT-K) was used for the purpose. Figure 2.7 (a) shows a photo of this instrument

The measurements from Bruker-WLI were done using the Phase Shifting Interferometry (PSI) mode at 20x

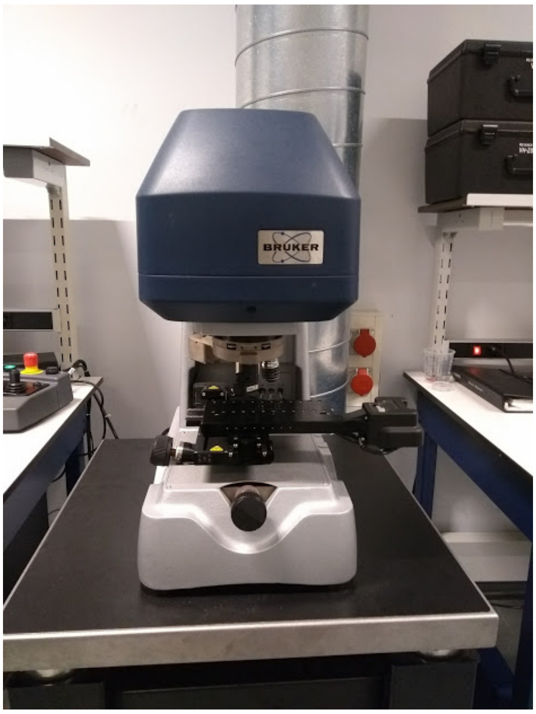

a

Figure 2.7: Photograph of Bruker ContourGT-K instrument

using a narrow band green light.

Once the measurement was taken using the Mach-Zehnder setup, the same droplet was also analysed using Bruker-WLI. The steps followed can be broken down as:

1. Dispense droplet of glycerol on a glow discharged glass substrate
2. Perform measurements from the proposed setup and take three readings. After recording each reading, switch off and back on the camera to measure repeatability. Time taken for successive measurements is three seconds and can be controlled using a custom-built MATLAB routine.
3. Remove the glass slide from the sample holder and quickly take measurements from the White Light Interferometer.
4. Wait for about 15 minutes and repeat steps 2 and 3

In the lab where these measurements were taken, the distance between the table where the proposed setup was built, and the White Light Interferometer is roughly 5 meters. Timestamp was recorded after each measurement. It took on average 2.37 minutes between the first measurement from the Mach-Zehnder setup and Bruker-WLI instrument. The maximum time difference was 3.2 minutes. From previous measurements, it was found that the height of the glycerol droplet reduces almost linearly at a rate of 6nm/minute. Thus, maximum evaporation loss is about 20 nm.

The detection limit of the proposed device can be found by monitoring the evaporation of the glycerol droplet continuously until it is completely dry. The smallest height at which the droplet profile is distinctly visible from the background noise and fluctuations is the detection limit of this system. Measurements were taken overnight with two minutes between successive measurements.

To test the feasibility of studying the dynamics of water layer on EM-grid, 0.1 μL of water was dispensed using a micropipette on the carbon side of the EM-grid. The grid was previously glow discharged for 2 min-

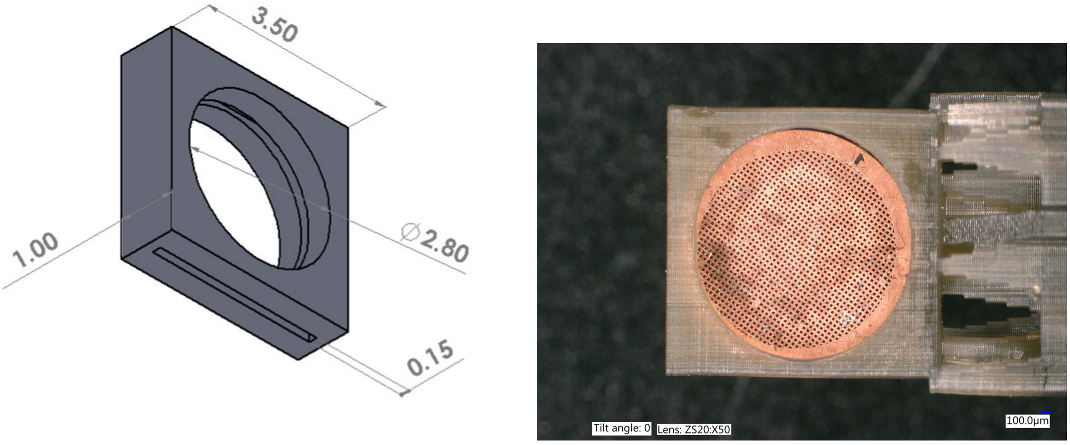

a

b

Figure 2.8: (a) Dimensions of the grid holder and (b) 3d printed grid holder (inset: grid holder with the finder grid)

utes at 10% power to make the surface more hydrophilic. The grid was soon mounted on the Mach-Zehnder setup and the evolution of interference fringes was recorded using the camera.

2.4. Results and Discussion

2.4.1. Simulation Results

Figure 2.9 shows the results from the simulation. The simulation conditions are as follows:

1. Reference droplet height: 300nm
2. Contact angle of droplet: 0.68 degree (contact radius = 50 micron)
3. Wavelength: 633nm
4. Number of pixels in interference fringes: 640 (width) x 480 (height)
5. Pixel size: 3.125 micron
6. Fringe visibility: 50
7. Simulated noise: Gaussian noise with zero mean and a standard deviation of 0.2 rad

The reference height profile in Figure 2.9 (a) is used to obtain the interference fringes shown in Figure 2.9 (b). The interference fringe is input to the SFFT algorithm which demodulates the phase to output the wrapped phase as shown in Figure 2.9(c). Height profile after unwrapping the phase and using Equation 2.8 is shown in Figure 2.9(d).

The result has a few important characteristics:

The unwrapped height profile matches the reference height profile quite well, as shown in Figure 2.9(e). However, there are two main regions where the reference height profile deviates from the wrapped height as seen in Figure 2.9 (f), which shows the difference between (a) and (d). One is the at the contact line of the droplet, where the difference between the reference and unwrapped height is about 20nm. This is the region where there is the maximum difference. The other is at the planar region where there is a noise of amplitude 10nm. Since the noise pattern is uncorrelated, it could be concluded that this roughness could be due to the Gaussian noise which is added to the reference height.

The location of the maximum error is an interesting result. The contact line is where the high frequency information is present in the signal. This information likely was filtered out in the SFFT algorithm. Thus, the edges of the unwrapped profile are smoother compared to the reference profile. This loss of information results in a reduction of height.

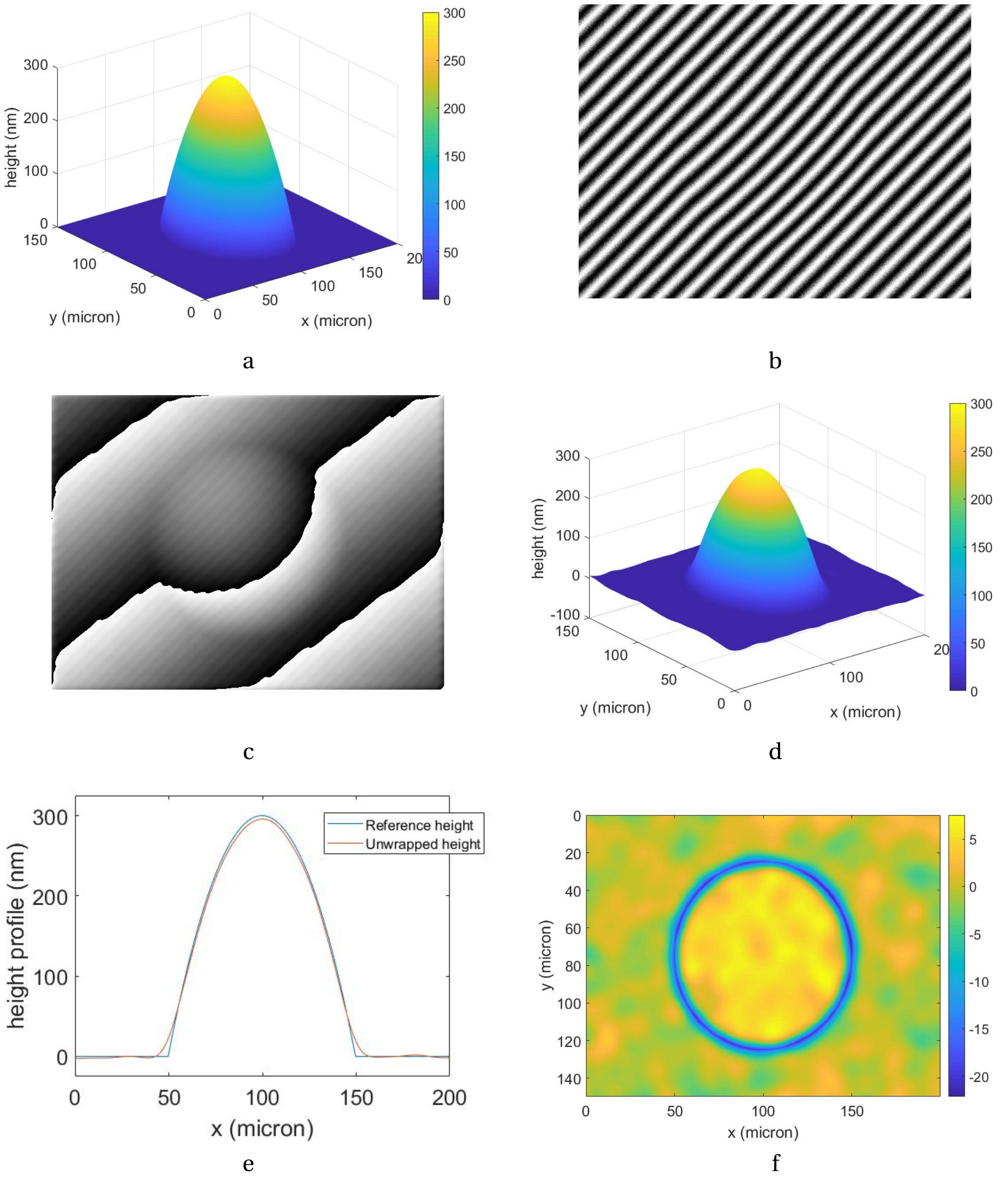

Figure 2.9: (a) Simulated result for a droplet having the (a) reference height profile at 300 nm height, and it's corresponding (b) interference pattern. (c) Wrapped phase obtained using SFFT (d) the unwrapped height profile. (e) Profile of the reference and unwrapped height profile at the maximum point and (f) the difference of (a) and (d)

The filter used to obtain this result is a Gaussian window with maximum value of 1 at one of the side peak. The filter width is 60 pixels and the Gaussian beam has a standard deviation of 12 pixels. Increasing the size of this window could reduce the error by adding higher frequency information to the analysis.

Figure 2.10 compares the reference height of a droplet to the value obtained after unwrapping for a range of input height between 100nm to 1000nm. The blue dots show the simulation results. The red dashed line shows the value obtained if the unwrapped result matched perfectly with the true reference value.

From Figure 2.10, the height of the droplet after unwrapping shows a linear trend when compared with the reference height. However, the linear trend has a slope less than one, suggesting that the SFFT is under-

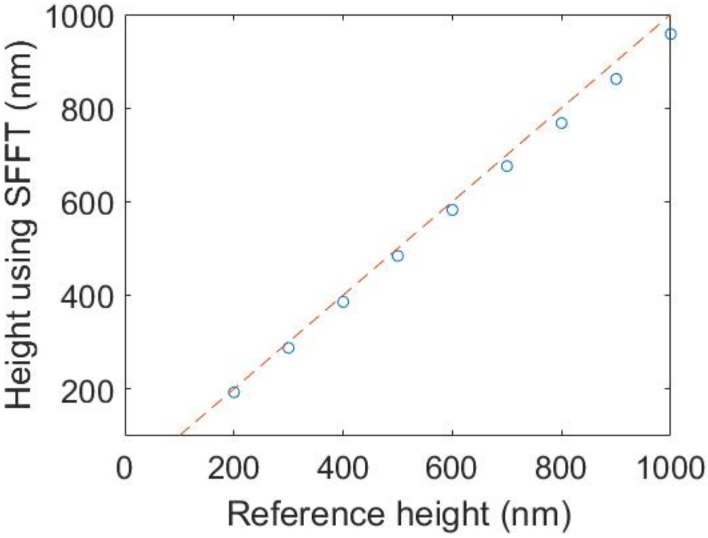

Figure 2.10: 4 Comparison of the reference height and unwrapped height using SFFT (blue circles) for a range of height between 100nm to 1000nm. Red dashed line indicate the reference height

predicting the height value. This is expected since the high frequency information is filtered using the Fourier window. This leads to a systemic loss of information. The loss of information can be quantified by dividing the reference height by the height obtained after SFFT. Doing that resulted in a value of 1.06. Thus, the loss of information due to filtering amounts to a 6% error in the height obtained.

2.4.2. Experimental Results

Figure 2.11 shows the result obtained when interference fringes were obtained experimentally.

Figure 2.11(a) shows the interference fringe captured by the CCD which was used as the input to the SFFT algorithm to obtain the wrapped phase shown in Figure 2.11(b). The topography result obtained after unwrapping is shown in Figure 2.11(c). Figure 2.11(d) shows the topography of the same droplet measured using Bruker-WLI.

Artefacts can be seen from the wrapped phase result as seen in Figure 2.11(b). These artefacts likely arose due to the following reason.

As mentioned earlier, the side peak is shifted to the center of the image after filtering. This is done to remove the background fringes and remove tilt. However, this process can also shift any signal near the zero frequency point by an amount equal to the carrier frequency. This shifting causes artefacts to appear in the wrapped phase. These artefacts causes distortions in the final result. Therefore, it needs to be filtered using a low pass filter.

The height map obtained using SFFT shows a relatively lower resolution compared to the result obtained using Bruker-WLI. The sharpness of the edge is reduced, which is likely due to the low pass filtering. To study the difference between the result obtained from SFFT with the bruker-WLI result, droplets of different heights ranging from 100nm to 1000nm are measured using both setups. Figure 2.12 compares the result obtained using these two methods.

Figure 2.12 reveals a systematic error being introduced in the setup. The error was found to be 26% relative to the measurements taken using Bruker-WLI. This is likely due to the fact that the unwrapped height map needs to be heavily filtered to remove the artefacts obtained during data analysis.

A solution to reduce this error is to avoid introducing artefacts in the setup. A possible way to achieve this could be to avoid shifting the peak to the center. The tilt introduced by not shifting the peak could be removed by finding a tilt plane which forms a least-squares fit with the planar region of the image. This tilt

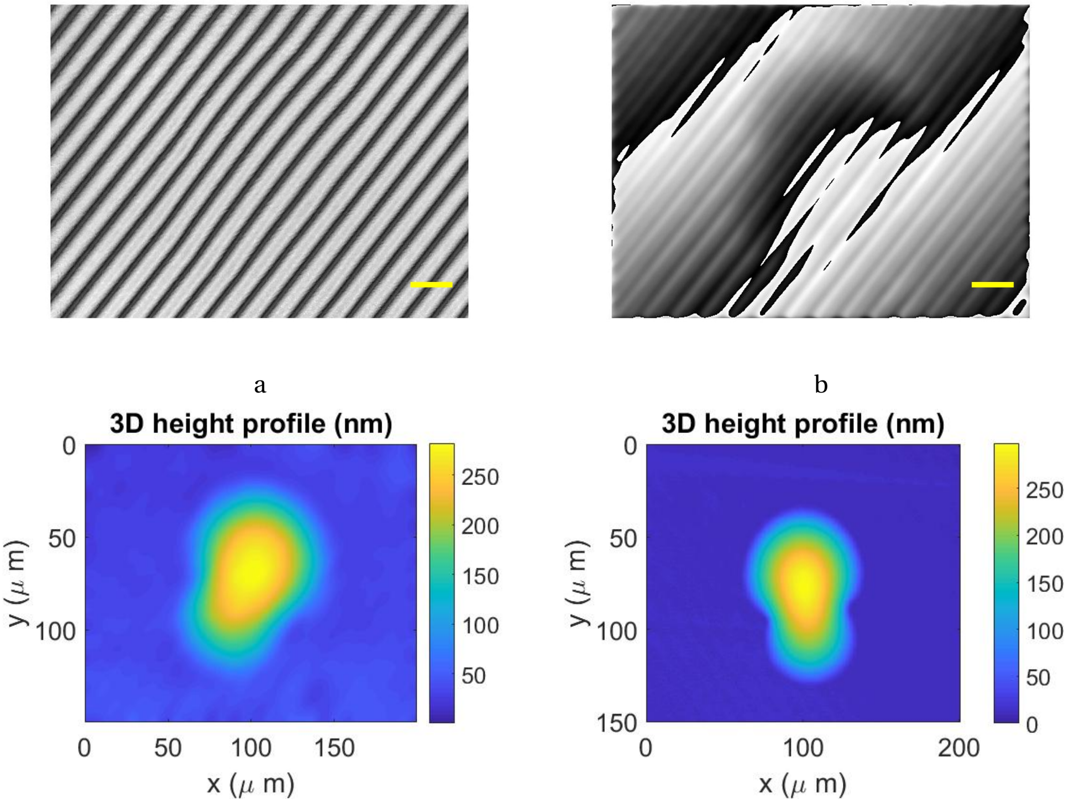
a

b

c

d

Figure 2.11: Experimental results showing the (a) interference fringe captured by the CCD, (b) the wrapped phase, (c) height map after phase unwrapping and (d) height map obtained using White Light Interferometer. Scale bar for (a) and (b) is 20 μm

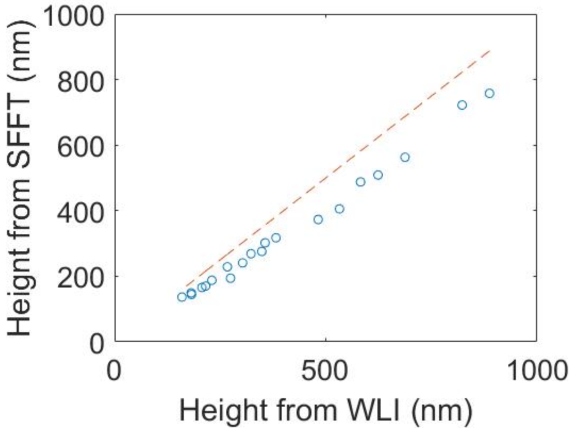

Figure 2.12: Comparison of the height obtained using WLI and using SFFT. Red dashed line indicate height from WLI

plane could be subtracted from the unwrapped height map to get a planar height profile.

The find out the repeatability of this setup, measurements from the proposed setup were taken three times and the average height map was obtained. The RMS difference between the three results is a measure of repeatability of the system. For all the measurements taken to obtain the curve shown in Figure 2.12, the mean value of repeatability was found to be 14.7 nm.

Reproducibility of the system is found out by taking measurements of a static structure at different intervals of time and at different environmental conditions. For this purpose, a droplet structure was 3d printed using Nanoscribe which has the same shape as that of a droplet. Figure 2.13 (a) shows the height profile measured using Bruker-WLI and Figure 2.13 (b) shows the height profile measured using SFFT. The structure was measured using Bruker-WLI on the first and last dates (12 sept and 14 Sept). The average height as measured from WLI was 2224 nm. The difference between the two measurements was 26nm.

Three readings were taken of the same structure at two different environmental conditions for three days. The environmental conditions were varied by switching on and off the ambient light. Figure 2.14 shows the results obtained for this study.

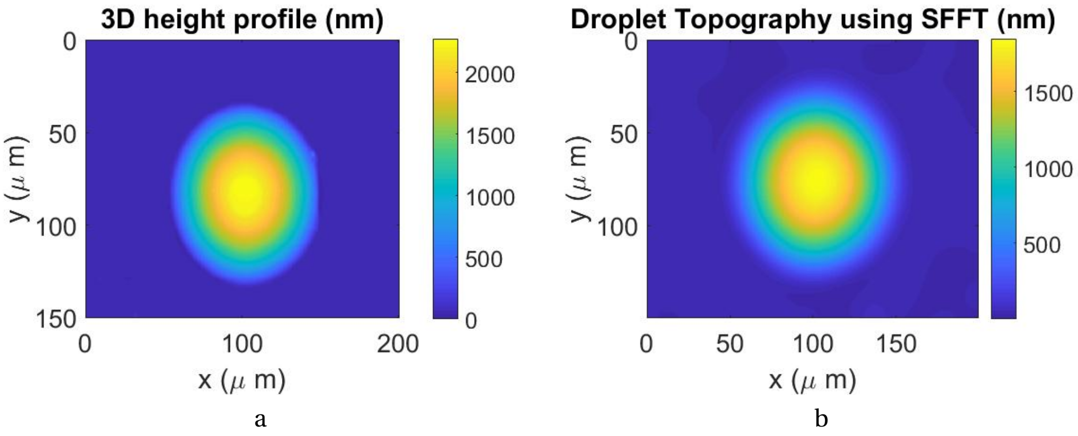

a

b

Figure 2.13: (a) True height map as determined by Bruker WLI and (b) Height map unwrapped using SFFT

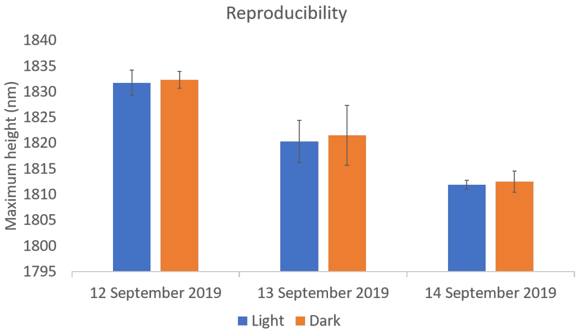

Figure 2.14: Maximum height measured on three days, in light and dark conditions. Three readings were taken and the error bars indicate the standard deviation observed

Changing the environment from light to dark has the effect of increasing the maximum height by about 1 nm. However this increase is much less compared to the repeatability of the instrument. Thus, the ambient lighting could be neglected.

There is a gradual decrease in the height measured due to drift as found by the change in the values over three days. This drift is constant for both light and dark conditions. The value of height measured drops by about 19.8nm over three days. Thus, the reproducibility of the setup is 19.8nm over three days. Further calibration can be done on the setup by using a standard specimen with a perfectly known height profile.

Figure 2.15 shows the result of an evaporation experiment for a droplet with initial height of around 2 micron. The height keeps fluctuating during evaporation. This is because of the dynamics of evaporation that takes place at the surface. On relatively short time scales, the droplet is not at equilibrium and constantly loses and gains mass. This results in the fluctuations seen in the curve. However, these fluctuations get reduced during later stages of evaporation when the droplet height becomes steadily linear. The evaporation rate was found out to be 0.4 pg/s. This is compared with the analytical model using the theory mentioned in [13]. However there was significant deviation from the experimental result, as the evaporation rate predicted by theory was 69 pg/s. Supplementary information 5.4 gives more insight into the details of this method, and possible sources of error.

Below a height of 165 nm, the height calculated is the same as the case when no droplet is present. This shows the detection limit of the proposed setup. At the inset of the figure, shows the height profile at three different moments. On the right side, the last few minutes of the evaporation is highlighted, and the scale bar of the droplet at 322 mins is adjusted to make it visible.

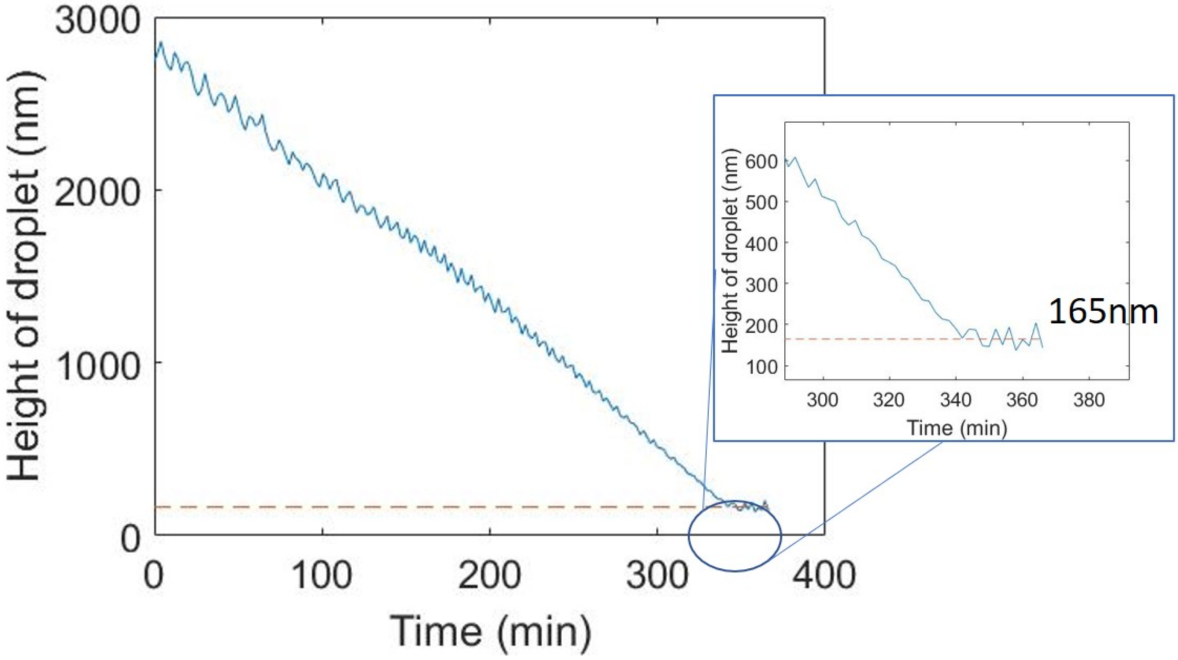

Figure 2.15: Height of a droplet during evaporation (inset: zoomed picture showing the final stages of evaporation). The ripple corresponds to the noise and background fluctuations

Experiments were performed to investigate the dynamics of a water layer on an EM-grid. Figure 2.16 shows the frames captured at different time intervals.

These frames show a gradual change in the curvature of the fringes which indicate the relative thickness of water layer between the center and the edge. This can be helpful to understand the breakup dynamics of a water layer on an EM-grid. Furthermore, it is observed that water starts to break from the center and proceeds towards the edge. It is possible to observe the edge of the water layer once this breakup happens. This information could be useful to obtain topography of the water layer in its final stages

Figure 2.17 illustrates the sequence which explains the behaviour of fringes observed in Figure 2.16. The thickness of water layer at the center of the hole is greater than at the edge in Figure 2.17 (a). As the droplet starts to evaporate, the curvature of the top surface becomes more flattened and at one point becomes equal to but opposite in direction to the bottom surface. At this point the fringe curvature should be zero and it should look like a set of parallel lines. After this point the thickness at the center of the hole becomes smaller compared to the edge, thus the direction of curvature changes. After a certain point, the two surfaces meet collapse and the breakup begins. The contact line then proceeds to move towards the edge of the hole.

2.5. Conclusion

Characterising microdroplets involves measuring its geometric properties. Recent developments in producing and manipulating such droplets have made it necessary to develop new ways of measuring the droplet

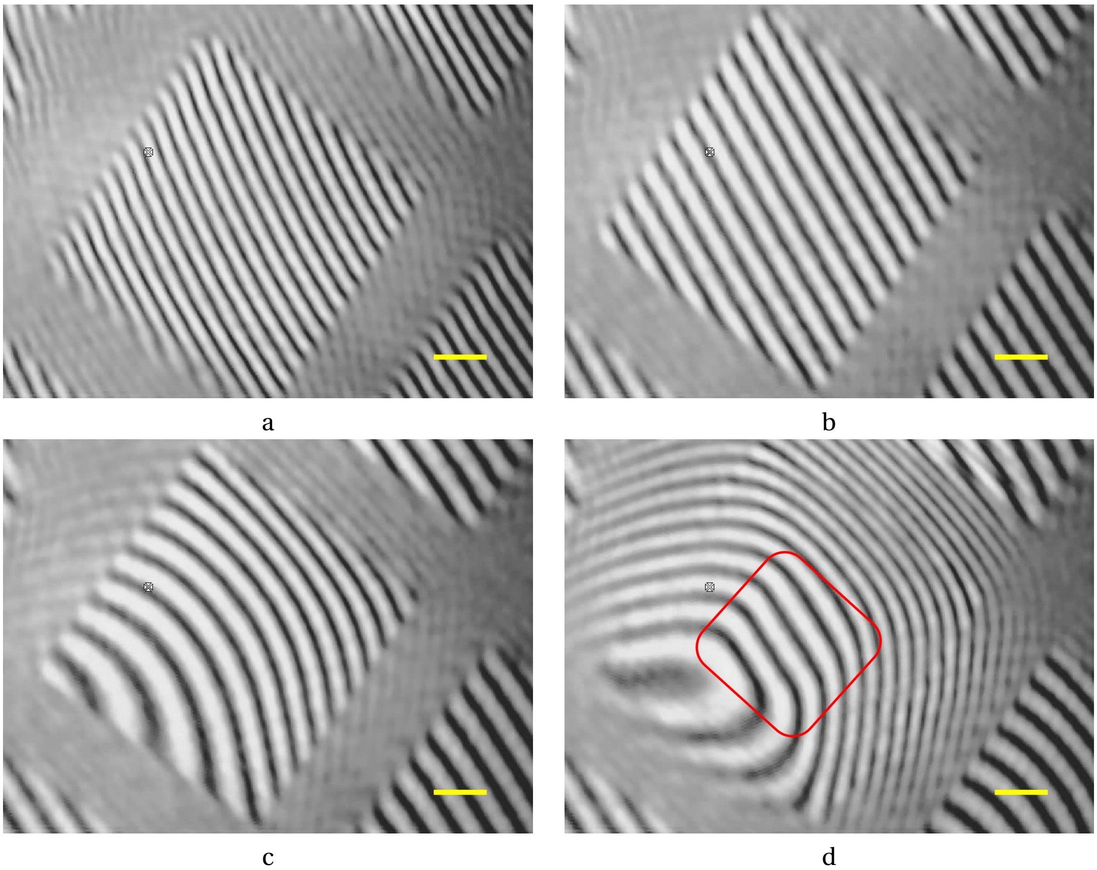

Figure 2.16: Gradual change in curvature obtained after a time interval of (a) 300s (b) 300.5s (c) 301 s and (d) 302 s Yellow box in (d) shows the edge of the water layer as the breakup proceeds towards the edge. Scale bar = 20 μm

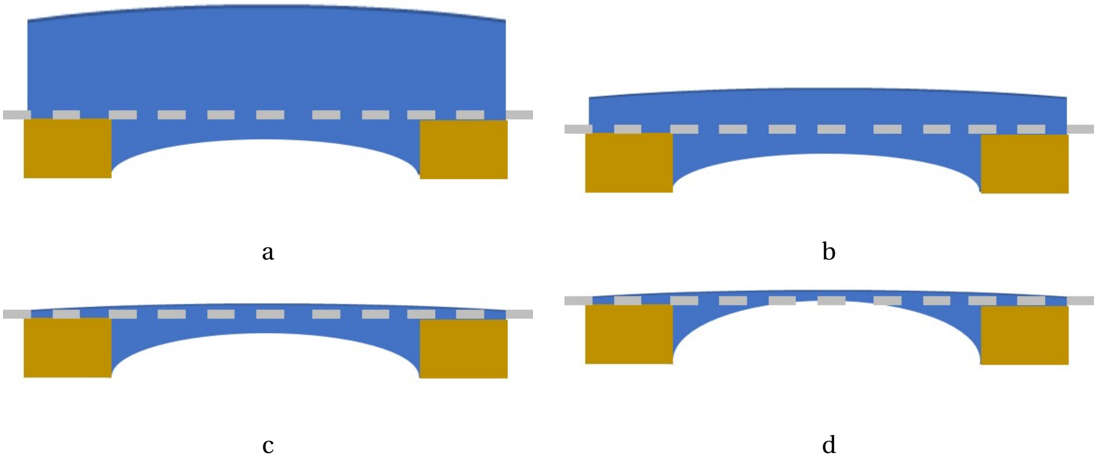

Figure 2.17: Schematic showing the gradual change in water layer surface for four different cases

geometry. Optical interferometry has been a popular technique for measuring droplet topography. This has been demonstrated through techniques such as Spatial Phase Shifting Interferometry and Temporal Phase Shifting Interferometry.

Fourier transform interferometry is a simple technique to obtain the phase from a single interference fringe pattern. This method has been employed before to study evaporation behaviour of droplets. However, the measurements taken from the setup was not characterised with another instrument. In this report, a method to validate these measurements by another instrument is explored.

A Mach-Zehnder Interferometer to obtain the interference fringes experimentally. Glycerol droplets having sub-picoliters volume were dispensed using a AFM cantilever on a glow discharged glass slide. To validate the results, a standard Bruker White Light Interferometer was used in PSI mode. By comparing the results, the proposed setup was found to have an error of 23%. The repeatability of the setup was 14.7nm and it had a reproducibility of 19.8nm over three days. The evaporation of a glycerol droplet with an initial height of 3 micron was studied through this setup by taking measurements at an interval of 2 minutes. The detection limit of the setup was thus found to be 165 nm.

The system was also tested with a large water evaporating on EM-grid. The final stages of evaporation could be studied in detail using just fringe analysis. However, currently the method has not been validated against cryo-EM due to time constraints. In future, droplets of glycerol will be dispensed on a cryo-EM grid and measurements will be validated. These results will inform the community about the effectiveness of optical interferometry to measure droplet topography even when the substrate is non-ideal.

3

General Conclusions and Outlook

A novel method of dispensing liquid droplets using hollow microcantilevers is useful for isolating bio-molecules from its environment. Once isolated, the desired bio-molecules could be studied in greater detail using an instrument such as Cryo Electron Microscopy. Thus, hollow microcantilevers are seen as a promising tool to develop samples for cryo-EM. However, one of the main challenge with implementing this technology is the high frequency of sample failure. Sample failure happens when the thickness of the ice layer on the EM-grid is too thick, and currently this failure is observed only after taking the sample to the cryo chamber

An approach to solve this key issue is to implement a measurement system which gives the topography of the droplets in real time. By monitoring the thickness of the sample it is possible to determine the exact moment when the EM-grid needs to be plunge frozen. This ensures that the ice layer thickness remains at a desirable level and therefore it is possible to avoid sample failure.

This report was aimed at developing a tool which could measure the topography of a low contact angle droplet. An optical system using interferometry is proposed as a concept. To demonstrate the effectiveness of this concept, the topography of a low contact angle glycerol droplet placed on transparent glass surface was measured. The proposed system was validated with a Bruker White Light Interferometer and it was found to have an average error of 23%. The detection limit of the device is 165nm. The setup had a repeatability of 14.7nm and a reproducibility of 19.8nm over three days.

The setup was used to observe the dynamic behaviour of water layer present on a glow discharged EM-grid. This was done by analysing the changes in the interference fringes within one grid square as the water layer evaporates. It was found that the break-up of water layer starts from the center of the grid square and proceeds towards the edge. This phenomena could be used to better predict the exact moment when the grid be plunge frozen to vitrify the sample. The solution could work not just in the cryo-EM sample preparation systems which dispense only a small droplet of water on a grid, but also for traditional systems where water layer occupies a much larger area.

3.1. Outlook

This project demonstrated that optical interferometry could be used to measure the topography of a low contact angle droplet. This was done by using a droplet-on-glass model where the droplet was supported on a clean and smooth glass slide. The next step is to demonstrate the principle when the droplet is supported on an EM-grid. Due to time constraints, these tasks could not be completed and are recommended for future works. The next section gives an overview of key steps that need to be taken in future.

3.1.1. Experimental methods for using EM-grid

Obtaining a glycerol droplet on an EM-grid using the technique described in Section 2.3.2 was difficult. It was found that the droplet did not flow out of the cantilever tip like it did on a glass surface. This maybe because the EM-grid surface is not hydrophilic enough to attract the droplet from the tip. However, increasing the glow discharge time is not possible because it would lead to etching of the carbon film from the grid. Thus, the following steps are recommended to dispense droplets on the grid.

1. Use ink-jet printer: It is possible to use an ink-jet printer to dispense ink droplets on the EM-grid without damaging the carbon film. The same method could be used to dispense glycerol droplets on a glow discharged EM-grid. Figure 3.1 shows the drop of ink dispensed on the EM-grid when mounted on the Mach-Zehnder interferometer. The contact angle of the droplet was too high to take any measurements from the setup. However, this could be resolved by glow discharging the EM-grid and dispensing glycerol droplets using ink-jet printing.

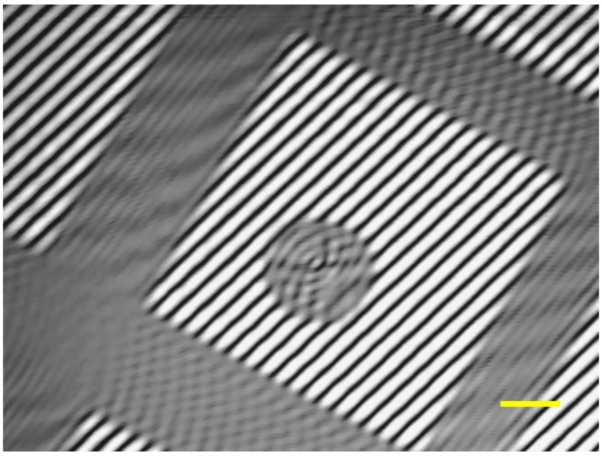

Figure 3.1: Droplet of ink dispensed on the EM-grid using an inkjet printer. The image is taken by the Mach-Zehnder setup. Scale bar = 20 μm

2. Use hollow microcantilever: The hollow microcantilever could be used to dispense glycerol droplets on the EM-grid. However, this has not been tried and may require some optimisation initially.
3. Use silicon coated EM-grids: The silicon coated EM-grids are available and they are more resistant to etching than carbon films are. This could be a used in conjunction with the AFM dispensing technique described in Section 2.3.

After obtaining a sample on the EM-grid, it can then be tested using the Mach-Zehnder interferometer setup. To obtain the topography result, a small change needs to be made in data processing. This is due to the presence of metal grids which do not add any information and could add noise to the signal. To avoid that, the square hole from the grid needs to be cropped and the cropped part is then processed using the SFFT algorithm.

3.1.2. Validation using CryoEM

The topography result obtained from the proposed setup needs to be validated with the cryo-EM measurements. However, for cryo-EM, the sample needs to be vitrified first. For the initial measurements glycerol was used as it had low vapour pressure. However it is not known whether a pure glycerol sample could be used as a sample for cryo-EM. The first question to answer would be how to vitrify glycerol droplets. If the same vitrification process and materials which are used for water droplets can be used for glycerol, then no major changes are required.

As such, it is difficult to test femtoliter water droplets on the grid without a significant loss due to evaporation. It takes time to set and align the sample with the optic axis and do the measurements. A humidity chamber maybe necessary to ensure the water droplets stay a much longer time. Once the measurements are taken for water droplets, it can then be plunge frozen into a liquid ethane bath and tested using cryo-EM.

An alternative would be to miniaturize the whole setup using a suitable optical design. Once miniaturised, the device could be fitted into the hollow microcantilever sample preparation setup which has already been built. The samples can be prepared using the hollow microcantilever setup and validated using cryo-EM after plunge freezing.

3.1.3. Real time Analysis

One of the main advantage of the SFFT algorithm is the short amount of time it takes for analysing the image. Using a HP Laptop, with core i7 processor (2.6 GHz) and 8 GB RAM, the SFFT algorithm and unwrapping algorithm together takes an average of 700ms to run. The input for the algorithm is an interference pattern with the droplet and without a droplet. However this time was calculated when the input variables were stored in memory, which makes it faster to retreive. In a real time application the time required would also need to take into account the data transfer rates through the USB ports from the camera into the computer.

Having a software which can process the data in real time would be the ultimate goal. The fact that the data processing time is 700ms is encouraging since there was no optimisation involved to reduce time. The program was built in a modular fashion. This made calling each different functions more time consuming. Thus more time could be saved by a better structuring the program and efficient data utilisation.

4

Reflection

This project was unique as it directly confronted a problem faced by the local research group in TU Delft. There was a very specific goal right from the beginning. From my perspective, working on a project which has a specific goal has both upsides and downsides.

The upside is it becomes easy to filter out different concepts. Thus, starting from an elaborate set of possible concepts, I could narrow it down to three different concepts and test them. In the first set of elimination, many thin film measurement technique were chosen. Some thin film measurement techniques, such as stylus profilometry, simply could not work based on the working principle. These were eliminated at the start. The few that were left had to be narrowed down further by a combination of literature review and calculations based on first principles. Such elimination was made easy as the goal was clearly specified.

A possible downside of having a specific objective is that it does not allow much for a plan B, in case a chosen technique fails to satisfy the requirements. Thus, it becomes necessary to divide the problem statement into clearly defined milestones right from the beginning. This project was therefore divided into two steps. In the first step, a droplet-on-glass model was chosen. This choice was motivated by the fact that it was easy to dispense droplets on glass, and have a validation tool which was readily accessible. The second step, a droplet-on-grid, model was not possible to test due to time constraints. However, since the first step was completed there is a clear sign of progress towards achieving the stated goals. Another downside is that there may be very little scope for novelty when doing a research targeting a specific problem. Novelty is usually measured by comparing with existing literature. In this project, the novelty criteria could be met only when both steps (droplet-on-glass and droplet-on-grid) were completed. Even though the development of a tool to solve the droplet-on-glass problem took a year worth effort, such techniques are already published in literature. However, taken in context, building this tool is a necessary first step towards achieving the stated goals.

One aspect of this project which helped faster progress was that all the components and materials needed to build a test setup are available in any standard optics lab. This was helpful because it enabled testing of different concepts in a short period of time.

Finally, there were some new and fascinating information that I got to learn through this project. It helped me develop a solid experience in both theoretical and experimental practice of research. The following section gives an overview of this.

4.1. Scientific knowledge gained

This project mainly involved the theory and application of optics to solve a measurement problem. Studying the following concepts proved very influential to the progress of this project.

4.1.1. Phase demodulation

One of the key ideas in this project involves demodulation of phase using Fourier transform. This idea was expressed in a paper published in 1982 which detailed the principle behind this technique. From then on, it has been applied on two dimensional fringe patterns using digital camera.

Phase demodulation is the process of extracting the phase information from an interference fringe pattern. Broadly speaking, phase demodulation techniques can be classified into two.

1. Using spatial carrier
2. Without using spatial carrier

The first method, which was implemented in this project, used a spatial carrier to demodulate the phase. This is similar to radio transmission in which the amplitude or a frequency of a carrier wave is modulated by a signal. In this case, the phase of a carrier wave is modulated by the signal. By taking the Fourier transform of the interference pattern it is possible to isolate the signal. This is the specific implementation of the spatial carrier technique which was chosen in this project.

Another way to demodulate the phase using information from the spatial carrier is to use sinusoid fitting method [29]. For this technique, the carrier frequency must be constant throughout the measurement, which is generally the case. By using the intensity measurements at three adjacent pixels in the CCD, the phase at the central pixel can be found out. This method is valid when the phase signal is assumed to be constant over three pixels.

The second phase demodulation technique doesn't involve a spatial carrier. The most common strategies involved in this are temporal and spatial phase shifting. Two or more interference fringe patterns are captured with a known phase shift between them. Information from these separate interference pattern could be used to demodulate the phase.

4.1.2. Dynamics of sessile droplet evaporation

The evaporation of a sessile droplet is governed by a diffusion process. The concentration of vapour molecules at the surface of a droplet is taken as the saturated vapour concentration, which can be found using the vapour pressure of the liquid. There exists a concentration gradient along the radial direction of the droplet. This gradient drives the evaporation process.

For a sessile droplet, the diffusion process is affected by the presence of a solid surface. This can be factored into the diffusion model using the contact angle. Thus contact angle plays a major role in determining the evaporation rate of a sessile droplet.

Learning about sessile droplet evaporation was important for two reasons. One, it was useful to have an idea of how the geometry changes with time. There are two modes of evaporation, with a constant contact radius or with a constant contact angle. A droplet placed on glass, or on any hydrophilic surface always evaporates in a constant contact radius mode. Second, since evaporation of sessile droplets is actively studied in literature, various techniques have been published to obtain droplet topography. The choice of using optical interferometry was mainly driven by the plenty of research papers which demonstrated this technique. These droplets had similar geometry and similar volumes to the droplets being studied in this project. Thus the optical interferometry was chosen as it had a good confidence.

4.2. Prior concepts studied

The selection of measurement concept was the first part of the project. Several concepts were investigated initially for their applicability to this project. Here is a brief overview of those concepts:

4.2.1. AFM Dipping Technique

A cantilever based liquid thickness measurement system is reported for polymer films [19]. In this technique, a cantilever tip is made to dipped through the liquid surface till it reaches the solid surface. The cantilever experiences a deflection when it meets both liquid and solid surfaces. The difference in height where the cantilever deflection is observed gives the thickness of the liquid film.

The cantilever technique can easily be adapted to our present case, since an AFM probe is already used to dispense the liquid droplet. Figure 4.1 explains the principles of this method.

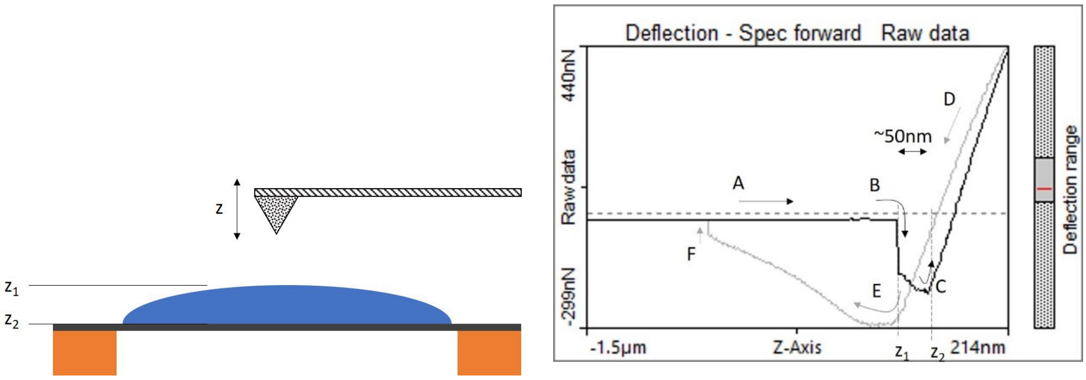

a

b

Figure 4.1: (a) Principle of the AFM dipping experiment and (b) a typical force distance curve obtained using the AFM

The accuracy of this method decreases with increase in film thickness, due to capillary effect which deforms the liquid surface. The main disadvantage of this technique is its slow operation. A single measurement takes few seconds time which can hurt the accuracy of the result due to rapid evaporation rates.

4.2.2. Capacitance measurement

Capacitance based thickness measurements are usually done for lipid bilayers and can measure thickness change up to few angstroms. The principle of the capacitance technique is to measure the change in capacitance due to a change in the length of dielectric medium present in between two parallel plate capacitors. A schematic diagram of this method is given in the Figure 4.2 (a).

Since capacitance (C) is proportional to the area of the parallel plate capacitors, the small sizes of the droplet pose a main challenge to this technique. Area (A) to distance (d) ratio for the present case is significantly lower than most commonly used capacitance-based measurement devices. This reduces the sensitivity of the instrument.

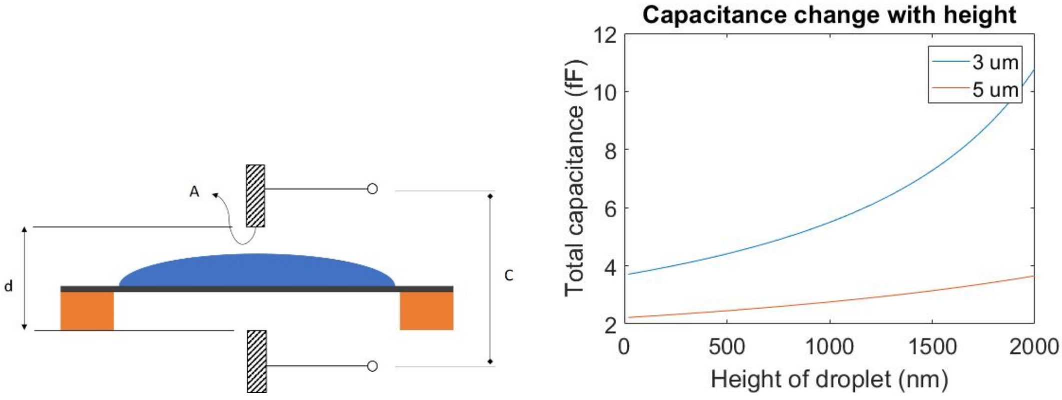

a

b

Figure 4.2: (a)Principles of capacitance based height measurements and (b) Analytical results for sensitivity analysis.

The sensitivity of the instrument over the given thickness range can be measured analytically using the formula for capacitance of parallel plate capacitors. Figure 4.2(b) shows the effective capacitance measured for different droplet heights. The distance between the capacitors are kept constant at 3 um and 5 um. We can see that as the distance (d) increases, the capacitance changes decrease and beyond 5 um it is not possible to measure a capacitance change over the given thickness range.

To increase the sensitivity, the plates must come very close to each other which adds the risk of collision with the copper grid. The effects from the fringe fields are ignored in this analysis, which is another disadvantage. The main upside with this technique is the fast response times, and smaller footprint.

4.2.3. Transmission spectroscopy

The Fresnel transmittance of an optical medium is dependent on its thickness, refractive index and wavelength of light. For a given sample, we can assume its thickness and refractive index to be constant. If we know the refractive index of the sample material, we can calculate the thickness by measuring the transmission spectrum. This can be done by several means. A direct method is to pass white light through a diffracting element and incident the light on the sample and measuring the spectral transmittance using a spectrum analyser. Since each thickness can produce a unique transmittance curve, the thickness can be obtained by directly comparing with a fitted curve using least squares method.

Figure 4.3. illustrates the principles of this method. To measure the efficacy of this method, a transmission curve was obtained using a known thickness. Random noise with 1% standard deviation was added to the curve and a least squares error was employed to retrieve the thickness by running a model over the full possible thickness range. This is shown in Figure 4.3 (b). The thickness for which the model predicts the best fit is chosen as the reconstructed thickness. The reference and the reconstructed thickness were found to have good match for 50 random reference inputs.

The transmission curves were obtained using the TMM tool (Transfer Matrix Method) developed by Steve Byrnes. The tool details and documentation can be found online [30].

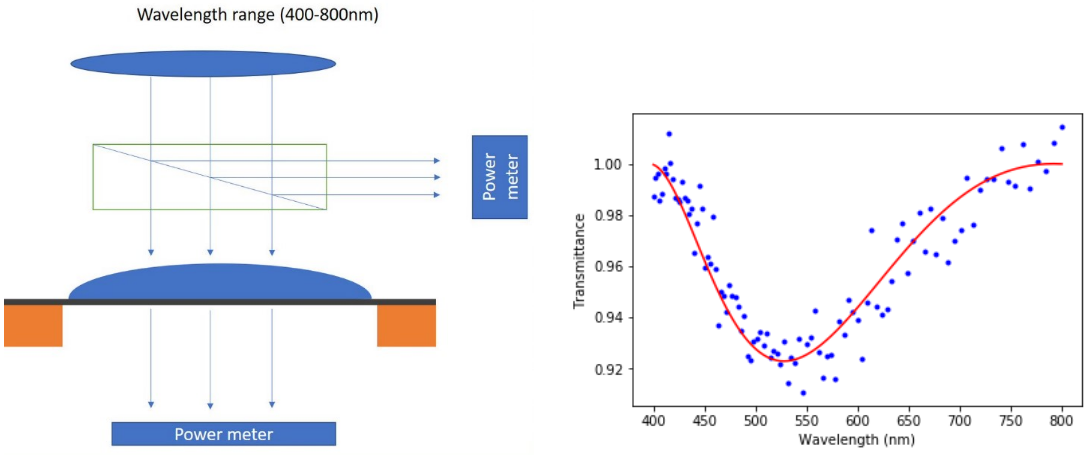

a b

Figure 4.3: (a)Principles of transmission spectroscopy and (b) Reconstruction for an input thickness of 300 nm using least squares fitting

4.2.4. General comments about concept selection

The concept selection was driven mainly by secondary factors such as the availability of components, prior knowledge and a demonstration of the concept in literature. It is best to compare different concepts studied above with interferometry against these criteria.

The AFM dipping technique was the best and the simplest among those considered. This is mainly due to the fact there was no need of any other new components and measurements could be made in principle with the hollow microcantilever which dispense the liquid droplet. However, two main disadvantage of this method is that it is slow, and it might contaminate the droplet as it has to be in contact with the droplet for measurements. This technique can be implemented when a point measurement is the only concern. In that case, the hollow microcantilever could be used to measure the droplet height at a single point and monitor after every fixed time period. An optical interferometry on the other hand, enables remote monitoring and does not affect the sample. It can also provide the topography of the droplet and not just point measurement at a much faster rate.

Capacitance method could be used when there is a sensitive enough capacitance sensor. Calculations from first principles indicate that the sensitivity of the sensor should be of the order attofarad. It is not clear if such sensors are available. Interferometry could be used with standard optical components found in any regular optics lab. This saves time in the later stages of project.

Transmission spectroscopy is very close contender with optical interferometry due to its simplicity. The calculations made from first principles suggest it should be possible to detect the thickness at a fairly decent resolution. However, these calculations were made by a simplifying assumption that the optical medium had a flat surfaces. However, in case of the liquid droplets there would be slight curvature due to the surface tension of the liquid. When the surface becomes curved, the angle of incidence for secondary refraction changes slightly and this will affect fresnel reflectance. Thus, it is not known if such a method was used for measuring height of droplets. Interferometry on the other hand takes advantage of the curvature of the droplet and provides a topography information over any selected area. This technique has been widely studied in literature and therefore was an appealing choice.

4.3. Prior iterations

Once it was decided to use optical interferometry, there still remained question on the specific implementation of interferometry. There are many types of interferometers available to obtain interference fringes. Therefore, a decision on the specific interferometry setup and data analysis technique had to be made.

Building an interferometer gave me an introduction to the practicalities of setting up experiments on an optical table. There are some key issue that I learnt are important. One is alignment. The optical axis of all the components need to be controlled meticulously. A good strategy would be to plan the layout first on a paper and then start setting up the components. The second issue I faced is slip and stick. Some ways of mounting optical elements are better than others. I found that mounting on a V-rail proved to be unstable due to stick and slip. I first mounted a lens on a V rail to be able to control its position. However, the screw which holds the base of the lens to the rail was not firm. It constantly slipped and caused vibrations which could be seen on the screen. A proper way to mount the lens was to bolt it down to the optical table, and control the position of the sample holder using a linear stage. Finally, drift was another issue which I faced. The drift was from the sample holder. The sample is held on to a vertically mounted XY stage with a magnet. Using only one magnet was not good enough as the sample slowly rotated about the axis of this magnet. This was crucial to measure the complete evaporation of a glycerol droplet which took 6-8 hours of time. To avoid the drift I used a two magnets placed next to each other to provide a counter moment. This was effective in reducing the drift.

Three interferometry setup were built and tested. They are explained as follows.

4.3.1. Michelson Interferometer

For the first iteration a Michelson interferometer setup was selected. It is a simple technique which has just few parts. The schematic of a typical Michelson interferometer is given in Figure 4.4 (a) and the photograph of the setup is shown in Figure 4.4 (b).

This scheme turned out to have some major problems and thus was discontinued. One problem was that when light passes through the grid, it forms a diffraction pattern as shown in Figure 4.4 (c). Much of the information is lost to the higher order diffraction elements. This could be improved by adding a lens to image the plane of the grid on the screen. This would limit the amount of information lost. However, in a Michelson setup, light passes through the sample twice. Only the zero-order light gets reflected along the same path and the diffraction caused by this light can be retrieved using a lens.

4.3.2. Dual Channel Simultaneous Phase Shifting Interferometer

This is a spatial phase shifting interferometry technique. Two or more fringe patterns are spatially separated and are projected on multiple CCDs. In a Dual Channel Simultanous Phase Shifting Interferometer, two CCDs

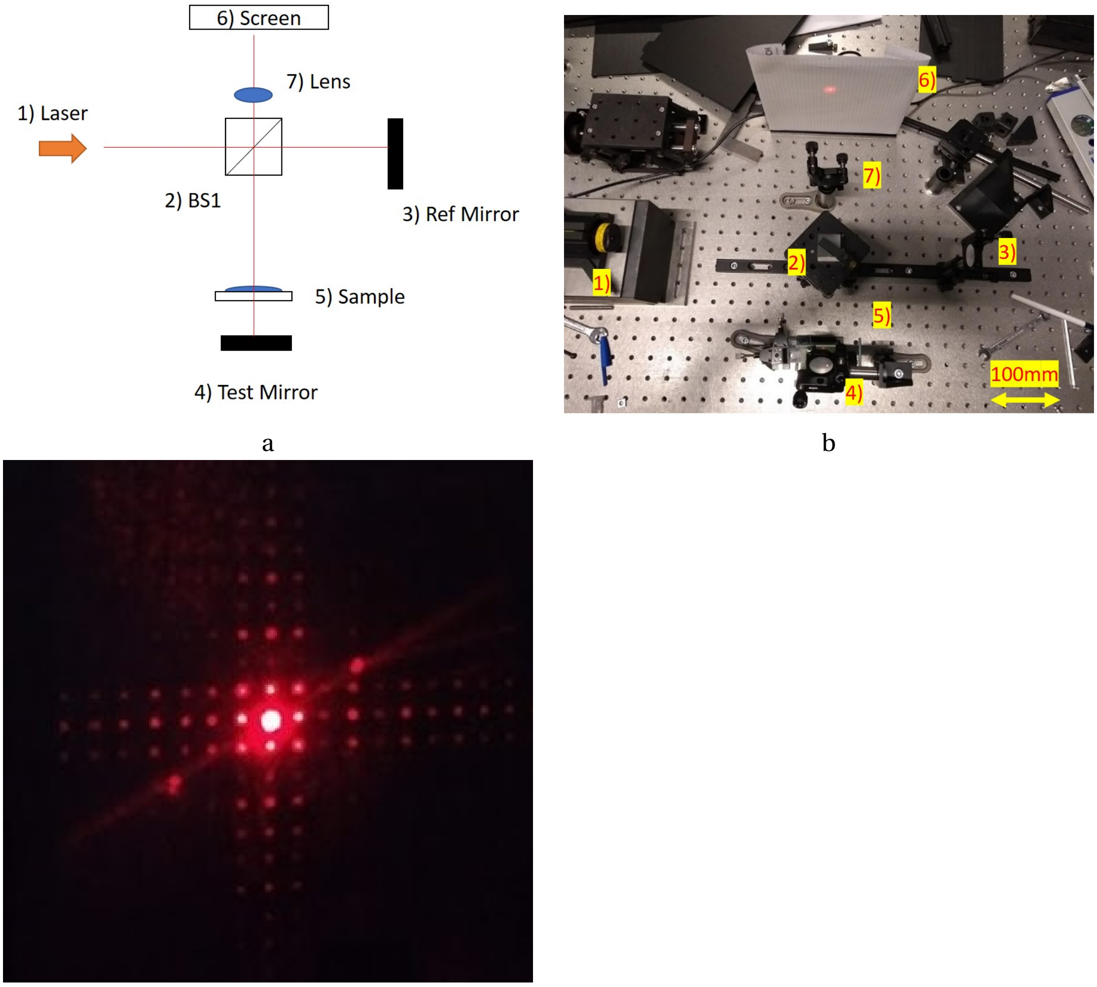

a b

c

Figure 4.4: (a) Schematic of a Michelson interferometer (b) photograph showing the completed setup (c) diffraction pattern observed when a grid is introduced

are used to record two interference pattern with mutual phase shift of $\pi/2$. The schematic of the setup is shown in Figure 4.5 (a) and the photograph of the completed setup is shown in Figure 4.5 (b).

This setup was built by taking the inspiration from P. Sun et al. [12] Light coming out of the laser is linearly polarised. The angle of polarisation can be controlled using a half wave plate (HWP). This light is then passed through a polarised beam splitter (PBS), which splits the incident light into two beams which are polarised in s and p directions. One of beam is sent through the sample and the other beam is sent through the reference arm. The sample plane is imaged on the CCD using an imaging lens L1. A second lens of the same focal length (L2) is added for wavefront correction. The two beams meet at the first non-polarised beam splitter (BS1). The two beams are then passed through the quarter wave plate (QWP) to obtain conjugated circularly polarised light. This light is then split using the second beam splitter (BS2) and gets projected on to the two CCDs after passing through a linear polariss (P1 and P2). By setting the angle of polarisation between P1 and P2 to be 45 degrees, the mutual phase shift of the fringe pattern between CCD1 and CCD2 is 90 degree. Once the two interference fringes are obtained, it is possible to get the wrapped phase signal with a simple equation.

However, the results from this setup is highly sensitive to misalignments in the setup. Any misalignment causes a relative shift in the position of the image between two camera. This shift can be seen in the Figure 4.6 (c) which shows the wrapped phase. An uneven profile is seen as a result of the misalignment. A relative shift of even 5 pixels causes drastic differences in the output as shown in the Figure (a).

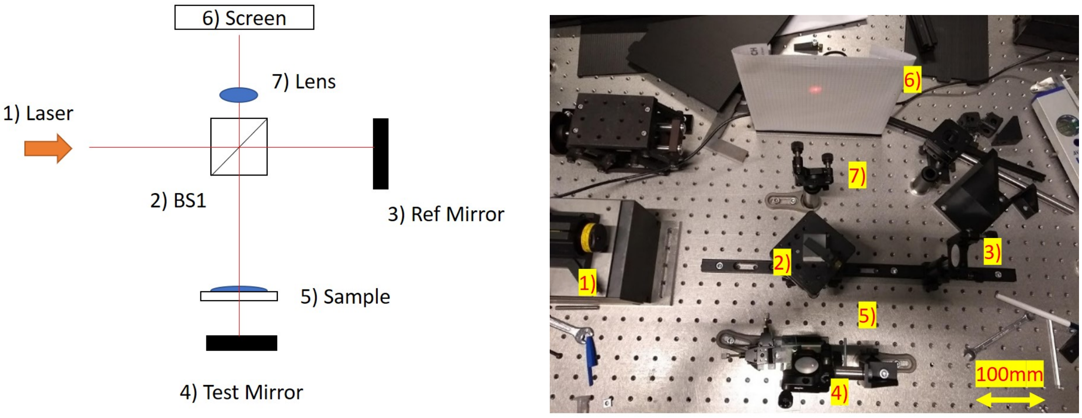

a b

Figure 4.5: (a) Schematic of the Dual Channel Simultaneous Phase Shift Interferometer [12] (b) Photograph of the setup

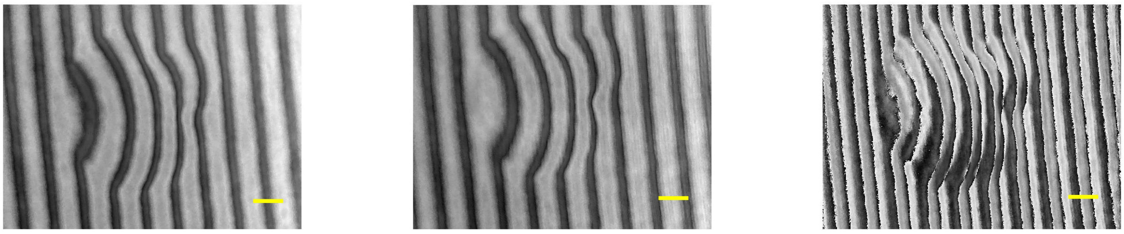

a b c

Figure 4.6: Interference fringe captured using (a) CCD1 and (b) CCD2. The two images were used to obtain the unwrapped phase (c). Scale bar = 20 μm

4.3.3. Mach-Zehnder Interferometer

The Mach-Zehnder interferometer is a much easier concept to build and test due to the lower number of components involved.

Temporal Phase Shifting Interferometry (TPSI) is a technique where one of the mirrors are moved in steps which are a known fraction of wavelengths. Two or more images can be captured using only a single camera with a precise control of its phase shift. Phase demodulation can be performed using suitable algorithms depending on the number of frames captured. This method offered an advantage over the previous method in that it is less sensitive to misalignments. However, a major drawback is the time taken to capture two or more phase steps.

Typically, the motion of a reference mirror is controlled with a piezo-actuator. Due to unavailability of such a piezo stage, another method had to be used to obtain the two fringes. It was observed that the fringe pattern could be moved slow enough just by manually pushing the reference mirror. A video recording of the moving fringes was taken at 15 fps. During post processing, two frames of the video were selected which had a mutual phase shift of $\pi/2$. The average fringe shift was measured for each frame relative to the first frame in terms of pixels. The frame which had a fringe shift equal to a quarter of the average distance between two fringes was selected along with the first frame for data processing. Figure 4.7 shows the two frames captured with a phase difference of $\pi/2$.

Figure 2.6 (a) shows the schematic of the Mach Zehnder interferometer. Since this technique does not involve two cameras, the problem of misalignment was avoided. Figure showed that the unwrapped height was indeed better than that obtained using DCSPSI technique. However, the base of the unwrapped profile was not a plane, but instead had a curvature. This may be because the video couldn't capture the exact frame where the phase difference was $\pi/2$ as it depends on the frame rate.

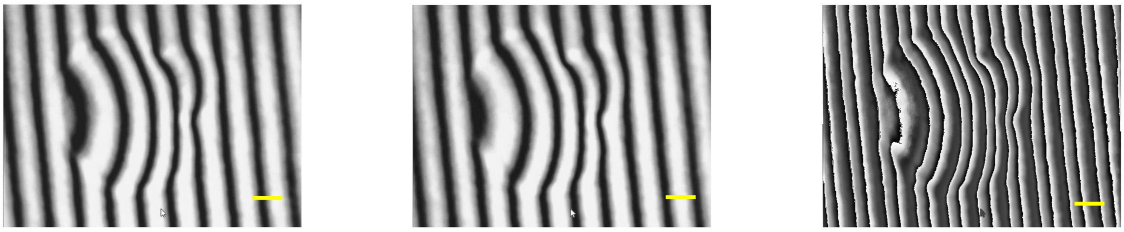

a b c

Figure 4.7: Demonstration of temporal phase shifting interferometry using two frames (a) and (b) having a mutual phase shift of $\pi/2$ to obtain (c) the wrapped phase. Scale bar = 20 μm

4.3.4. Comparison with SFFT

The SFFT technique had the advantages of both the above technique, in that it was simultaneous and insensitive to misalignments. This is because this technique uses only one camera and could record fringes continuously.

Figure 4.8 compares the results obtained by the three techniques.

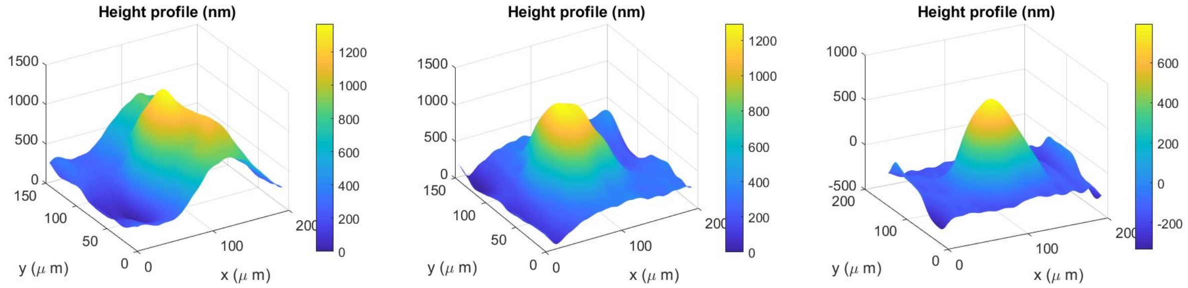

a b c

Figure 4.8: Surface height profile obtained using (a) DCSPSI, (b) TPSI and (c) SFFT techniques

Clearly, using the SFFT technique was better compared to the two. This can be seen in the proper way in which the droplet shape was unwrapped. One of the biggest reason for the unwrapping to fail for DCSPSI technique is misalignment. In principle this could be mitigated by using a cross-correlation algorithm in post processing. However, even the best result that was obtained with this method was just as good as the SFFT technique. The TPSI technique also has a lot of promise to unwrap the right shape of the droplet. The way in which this method was executed in this project was not optimal, as the movement of fringes was done by hand. There could be many parasitic signals which could arise due to this method. But even then, the shape of the droplet was unwrapped quite well. However, the benefits of using a single frame using the SFFT technique far outweigh any potential benefit from TPSI technique, especially when dynamic phenomena have to be measured.

4.4. Evolution of the project

Table 4.1 summarises the evolution of the project over the course of the past one year. The main outcomes of each quarter is listed.

Table 4.1: Evolution of project over past year

Period	Outcome
Oct 2018 - Dec 2018	1. Brief literature review on thin film thickness measurements 2. Initial calculations for AFM dipping technique, capacitance technique and transmission spectroscopy
Jan 2019 - March 2019	1. Literature review on droplet measurement techniques 2. Geometry analysis on the shape of a sessile droplet
April 2019 - June 2019	1. Interference fringes obtained using simulations 2. Data processing for DCSPSI successful for simulated fringes, but not for experimental fringes 3. Building and testing of interferometers on optical table
July 2019 - Sept 2019	1. Finalised setup: Using Mach-Zehnder interferometer 2. Data processing successful using SFFT algorithm, tested both for simulated and experimental fringes 3. Report writing and defense

4.4.1. Comments on best practices

Figure 4.9 shows the timeline of the project as originally planned.

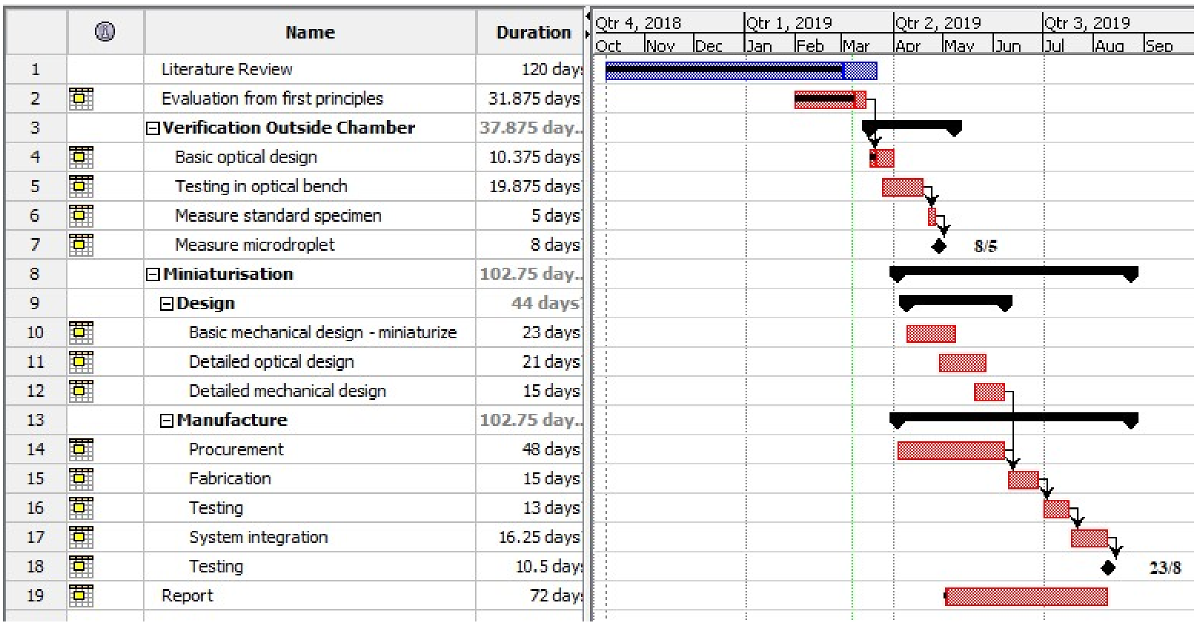

	ⓘ	Name	Duration
1		Literature Review	120 day
2	▦	Evaluation from first principles	31.875 days
3		**⊟Verification Outside Chamber**	**37.875 day..**
4	▦	Basic optical design	10.375 days
5	▦	Testing in optical bench	19.875 days
6	▦	Measure standard specimen	5 days
7	▦	Measure microdroplet	8 days
8		**⊟Miniaturisation**	**102.75 day..**
9		**⊟Design**	**44 days**
10	▦	Basic mechanical design - miniaturize	23 days
11	▦	Detailed optical design	21 days
12	▦	Detailed mechanical design	15 days
13		**⊟Manufacture**	**102.75 day..**
14	▦	Procurement	48 days
15	▦	Fabrication	15 days
16	▦	Testing	13 days
17	▦	System integration	16.25 days
18	▦	Testing	10.5 day
19	▦	Report	72 day

Figure 4.9: Timeline of the project as planned originally

The project was initially started with a goal of designing and building a device which could be implemented on the hollow microcantilever setup. However, within one year the progress achieved is behind expectations. The main reasons behind this was inadequate practical knowledge on building optical setup, mistaken assumptions and a general lack of planning. It was found that short term problems became overwhelming relative to long term project goal. In future, this should be avoided.

Other than these hiccups, there were some good practices employed which proved quite effective in pushing the project forward. One of the best practices was to use simulations to predict the performance of a given algorithm. In case of optical interferometry, simulations were done using a custom built MATLAB program which could show the type of interference fringe to be expected for a given droplet size. The knowledge of droplet geometry and evaporation behaviour proved useful at this stage. Another good practice that was employed was to have an extensive literature review in the beginning. This helped to direct the progress of the project in case there was failure at any point.

5

Supplementary Information

5.1. Illustration of Phase Demodulation for 1-D Interference Fringe pattern

Figure 5.1(a) shows the reference height profile for a droplet height of 1000nm. The length of the image is 2 mm. Figure 5.1 (b) shows the modulated fringe pattern, which has a carrier frequency of 8000 m-1. The size of pixel is 3.12 microns, and the number of pixels equal 640. Figure 5.1 (c) shows the three peaks in the Fourier transform corresponsing at locations $-f_x$, $+f_x$ and 0. The side peak at $-f_x$ is filtered in using a bandpass filter centered at $-f_c$. This is then shifted to the center of the spectrum to remove the carrier information. Taking the inverse Fourier transform we get a complex number, which has a phase profile as shown in the Figure 5.1 (d). This is the wrapped phase of the signal. After unwrapping and translating phase into height values, we get the unwrapped height profile.

5.2. Effect of Demodulation Parameters

The result of phase demodulation using SFFT is affected by the choice of the following parameters. This section is devoted to investigating the effect of each of the parameters on the result of phase demodulation. Simulated interference pattern is used for this investigation as it is easier and more reliable to compare the output with the reference input.

The parameters which affect SFFT are:

1. Filter Shape
2. Filter Width
3. Carrier Frequency

5.2.1. Filter Shape and Filter width

Two different filter shapes profiles are investigated: Top Hat profile and a Gaussian profile. Figure 5.2 shows the two different shapes studied.

It was found that the result obtained from SFFT is sensitive to the size of the filter used. Too large a filter size would leak information from the second peak, and too small a filter size would cause a loss of information.

This sensitivity could be reduced by choosing a filter of the right shape. A top hat filter is the most commonly used for SFFT applications. However, the sharp cut off from its edge causes undulations after performing the inverse transformation. A gaussian profile has the advantage that the shape remains the same for forward and inverse transformations, and there aren't undulations after inverse transformation. Figure 5.3 shows the effect of filter shape on the sensitivity of SFFT analysis

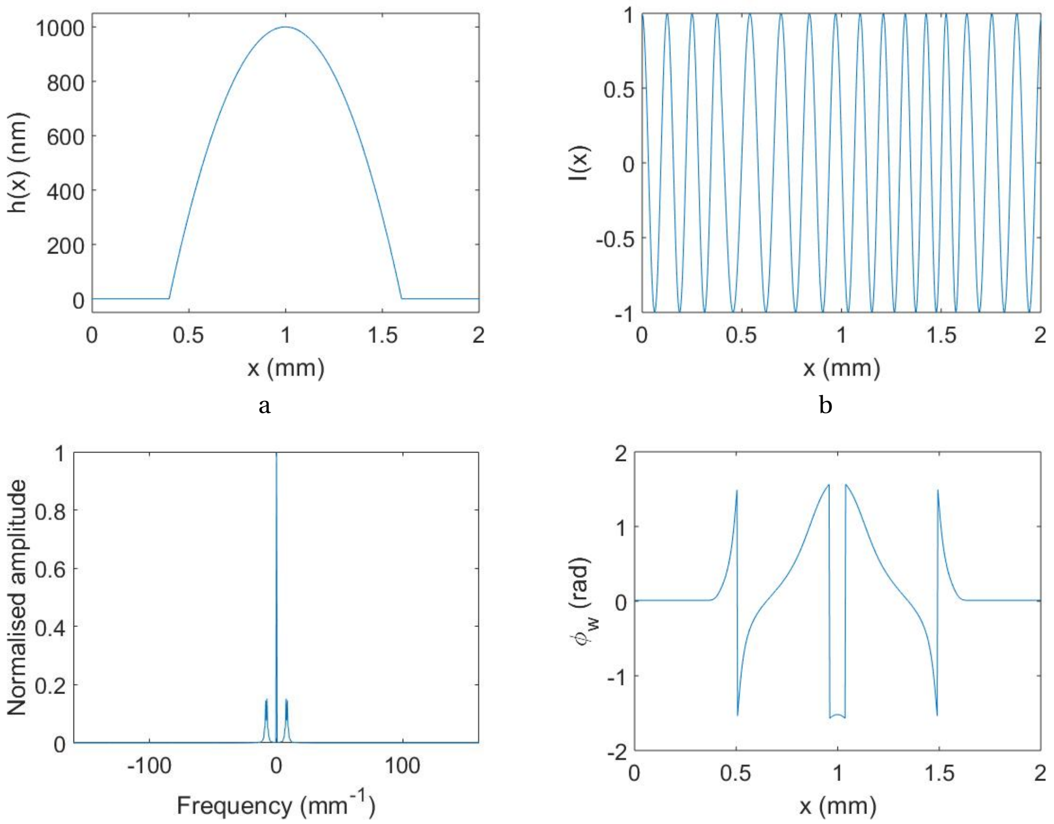

a b

c d

Figure 5.1: (a) Reference height profile for 1000nm max height (b) 1-D Interference fringe pattern (c) Normalised magnitude of Fourier transform and (d) wrapped phase obtained after demodulation

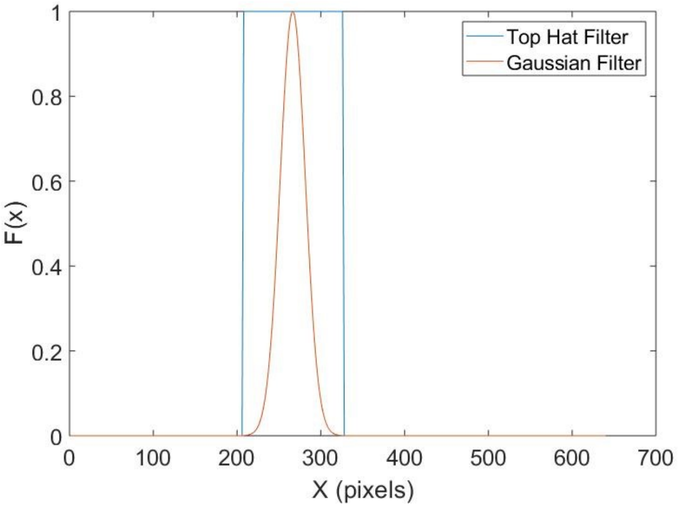

a

Figure 5.2: Two types of Filters used: top hat (blue) and Gaussian (red)

Simulated interference fringes for a reference droplet height profile of 1000nm was obtained. These fringes were input to a SFFT algorithm with (a) top hat filter and (b) gaussian filter profiles. The difference between the reference and unwrapped phase profiles was obtained. The maximum value of this difference was used as an indicator of the quality of phase demodulation and unwrapping.

Figure 5.4 shows the variation of maximum error as the filter size increases. It can be seen that for both filter shapes, there is a range of filter size where the error is minimum and stays constant. However, the range for the top hat profile is much smaller (30 pixels) than for the gaussian profile (150 pixel). This indicates that using a gaussian profile for filtering the peaks in the spectrum can reliably demodulate the phase, for a wide range of filter sizes.

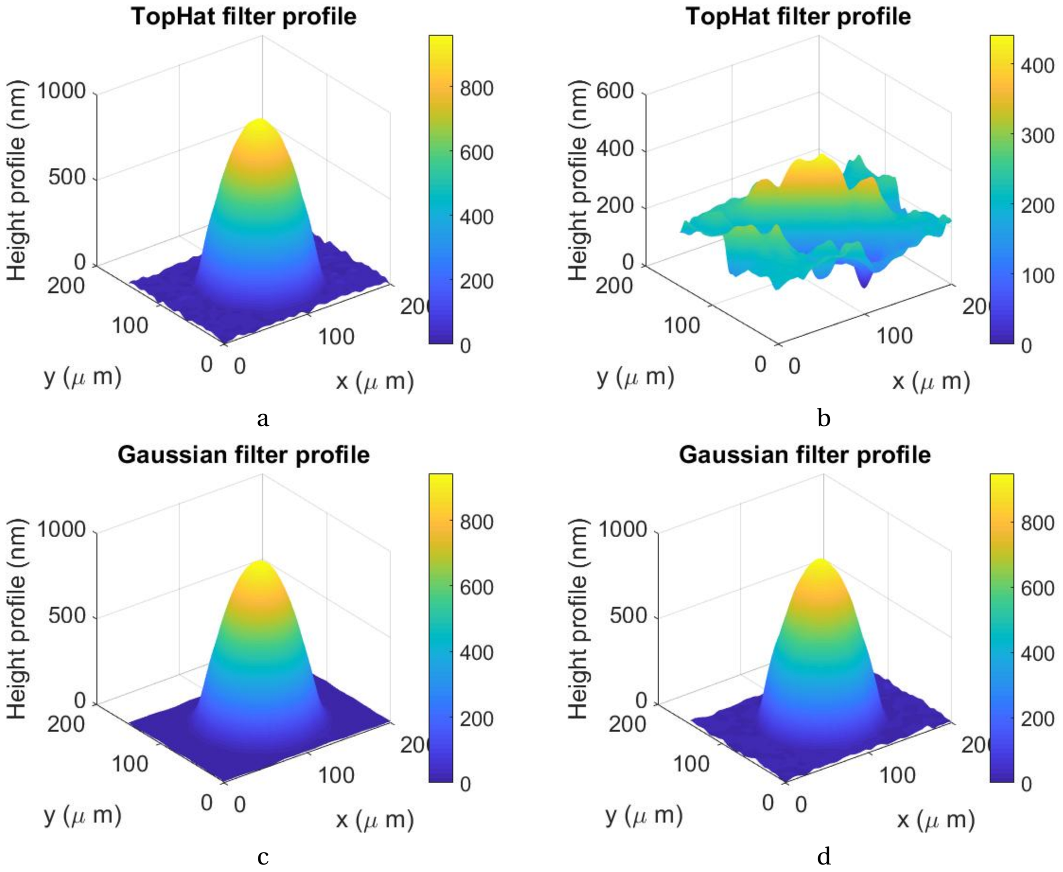

a b

c d

Figure 5.3: *Top row:* SFFT result using top hat profile with width (a) 20 pixels (b) 80 pixels. *Bottom row:* SFFT result using Gaussian profile with width (a) 20 pixels (b) 80 pixels.

5.2.2. Filter width and Carrier Frequency

The choice of the filter width is also affected by the carrier frequency. For higher carrier frequencies, the two peaks in the spectrum are further apart. Therefore it is possible to use larger filter size at higher carrier frequencies. Figure 5.5 shows the heatmap for a Gaussian filter and top hat filter profile. It can be seen that a higher carrier frequency and a moderate filter width is desirable in either case. However, after a certain size, the gain produced in lowering the error remains almost constant.

5.3. Phase Unwrapping

The result obtained by SFFT is a wrapped phase. The phase information is wrapped between $-\pi/2$ and $\pi/2$. The process of obtaining the full phase field from the wrapped phase is called phase unwrapping. Two algorithms are considered:

1. $2\,\pi$ phase stepping

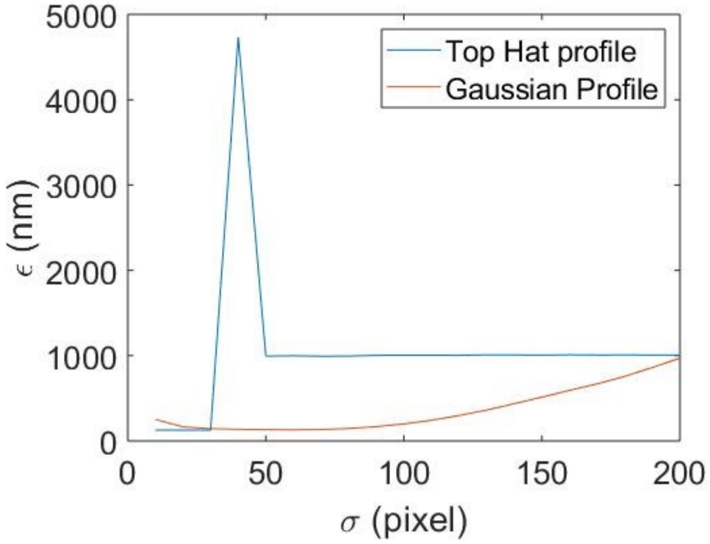

Figure 5.4: Error curves obtained for using Top hat profile (blue) and Gaussian (red) filter profiles

2. Volkov integration

2 π phase stepping is a popular method of unwrapping the wrapped phase. It looks for sharp jumps in the wrapped phase, which are more than a certain threshold (usually π or $\pi/2$) and adds 2 π at these points. The algorithm can be run either row-wise or column-wise.

It was found that the 2 π phase stepping method was quite unstable and produced artefacts near the edge of the output. The reason for this artefact is not clearly known. Thus, a different unwrapping algorithm proposed by Volkov et. al. [31] is used. Here, the wrapped phase field is used to get the gradient of the true phase field. This gradient information is integrated in the Fourier space to obtain the full phase field. The MATLAB implementation of this method can be found online [32].

The Volkov integration method produces undulations in the planar region of the unwrapped result. These limit the lowest detection limit of the method. Hence, it is preferred to use the 2 π phase steping method, once the cause of edge artefacts are identified and solved. The difference in the two methods is clear while unwrapping the wrapped phase shown in Figure 5.6 (a). Figure 5.6 (b) shows the edge artefacts produced by the 2 π phase stepping method and Figure 5.6 (c) shows the same wrapped phase un wrapped using volkov integration method.

5.4. Evaporation Rate

Evaporation rate can be calculated analytically using the Equation

$$\frac{dm(t)}{dt} = 4r_c D\frac{P_s M}{RT} \tag{5.1}$$

Where m is the mass of the droplet, r_c is the contact radius, D is the diffusion coefficient of the droplet in air. P_s is the vapour pressure of the droplet at temperature T and M is the molar mass. R is the universal gas constant.

The measurements were taken at room temperature of 293K. A glycerol droplet having a contact radius of 46 μm and a height of 2 μm has an initial mass of 9.2 ng. Diffusion coefficient and vapour pressure of glycerol was taken from [18] and the values used were 5 mm^2/s and 1.99 Pa respectively. Using these values, the rate of evaporation was found to be 69 pg/s. This would predict that the total evaporation time for a 9.2 ng droplet is about 130s. However, the droplet evaporation time was found to be 340 minutes, which gives an evaporation rate of 0.4 pg/s. Thus, the actual evaporation rate is about two orders slower than the predicted

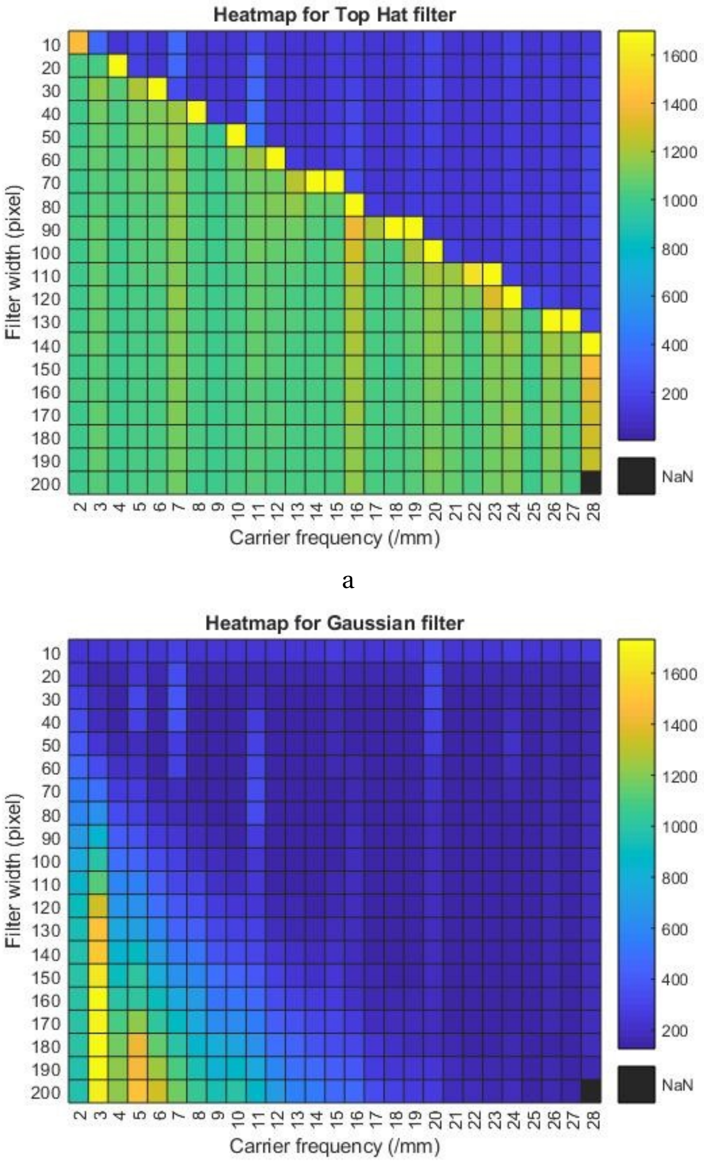

a

b

Figure 5.5: Heatmap of carrier frequency and filter width for(a) Top hat filter shape and (b) Gaussian filter shape

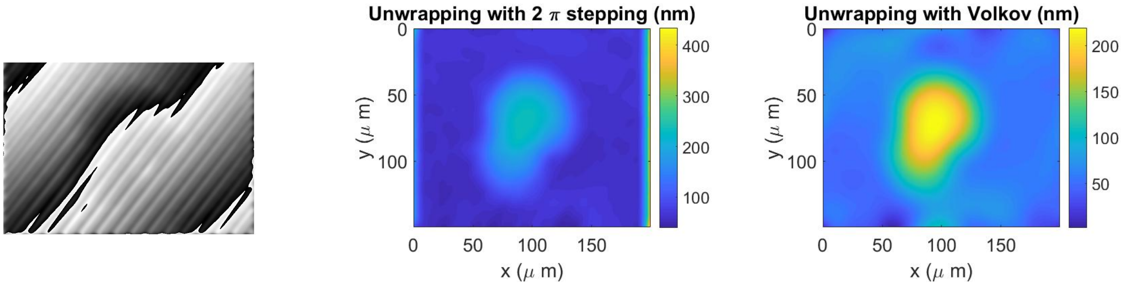

a b c

Figure 5.6: (a) Wrapped phase field for a droplet of height 200nm unwrapped using (b) 2 π phase step and (c) Volkov integration method

rate. This may be due to contamination which might have altered the material properties of glycerol.

Although the predicted evaporation rate is lesser than the experimentally determined evaporation rate by two orders of magnitude, the rate at which mass of the droplet evaporates is linear. This result matches with the predictions made by [13], which predicts a linear decrease in mass for droplets having contact angle less than 40 degree. This implies for low contact angle droplet, the effect of contact angle on the evaporation rate is negligible.

To remove any possible effect the setup might have had on the evaporation rate, the droplet evaporation was studied using the Bruker-White Light Interferometer. The evaporation rate found using this instrument was 0.8 pg/s, which is closer to the value obtained using the proposed setup than the analytical value.

To test whether the laser heating influences the evaporation rate of the droplet, a simple experiment was performed with the Bruker WLI. The droplet evaporation was monitored in distinct stages. First the droplet was under constant illumination by the green laser light of the WLI instrument for 40 minutes. During this time, measurements were taken at a regular intervals of 2 minutes. After 40 minutes, the stage which held the droplet was moved to a different location so that the droplet, or the glass which supports it, was under illumination. After this dark period of 40 minutes, the droplet was again bought under the illumination for another 40 minutes and so on.

Once all the measurements were done, the droplet volume versus time was plotted. It was expected to have data points only for those time when the droplet was under illumination. Figure 5.7 shows the result.

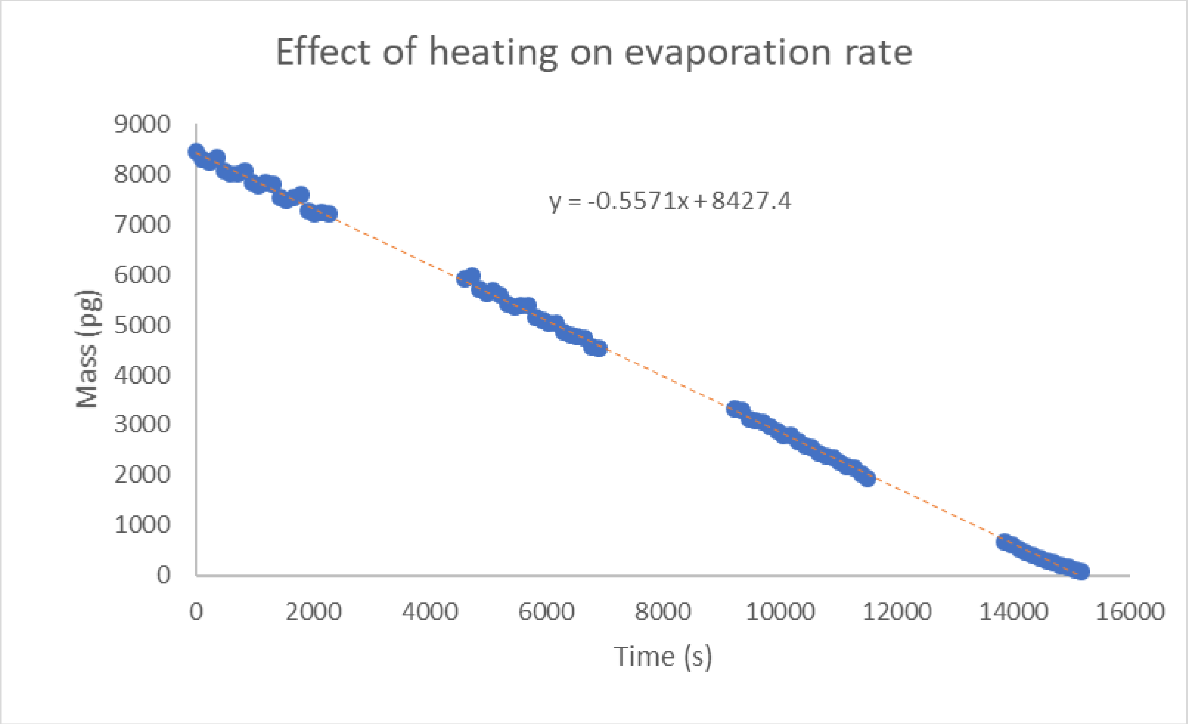

Figure 5.7: Effect of heating on the evaporation rate. The blue data points corresponds to the time when the droplet was under illumination and the red dashed line is the linear fit of all the data points

It can be seen that there are three "light" phases and two "dark" phases of measurements. The slope of the lines corresponding to the three "light" phases is the same as expected. If the illumination had any effect on the evaporation rate, then the droplet evaporation rate in the dark phase must be different. If that was the case, then there should have been an offset between the first light phase and the second light phase. As seen in Figure 5.7, there is no such offset. Thus, the evaporation rate in the light phase and the dark phase are said to be constant. This means the illuminating laser has negligible effect on the evaporation rate.

6

Appendix

6.1. Cleaning procedure for glass

First select a microscope slide, clean using a tissue so visible dust marks are wiped.

Table 6.1: Steps to follow to perform cleaning of glass slide

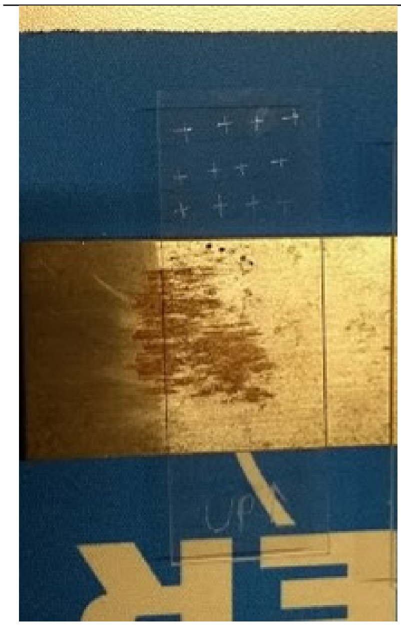	Make a marker, an arrow and a word “UP” to indicate the top surface where droplet is dispensed; and a cross to dispense a droplet. Press against the glass slide gently to scratch the surface just enough
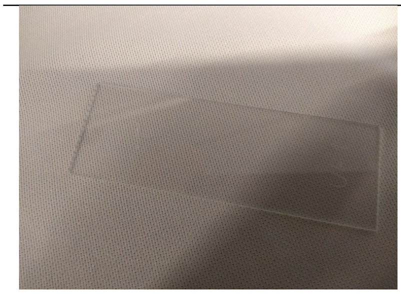	Place the slide on a clean-room tissue spread on a table. Gently wipe the surface first with a tissue wetted with DI water, and then with IPA. Use gloves.

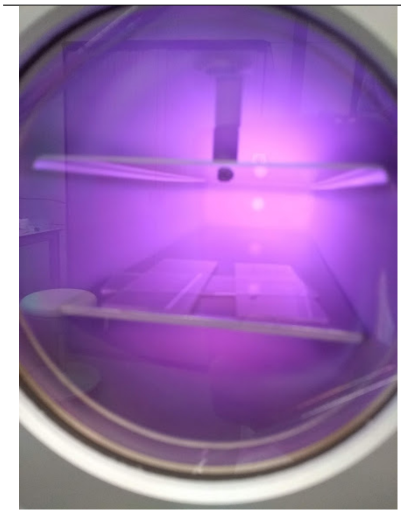

Switch on the plasma cleaner, and follow steps mentioned in plasma cleaner handbook. Make sure when the slides are inserted, the top surface of the glass slide is facing up . Parameters are: (1) Time = 25 mins, (2) Power = 99% or maximum.

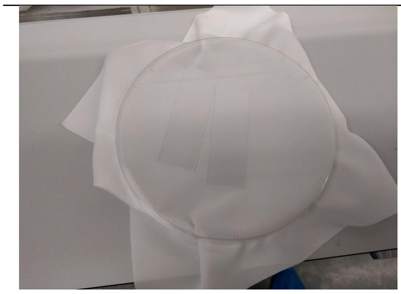

Remove the glass slide from the chamber. Quicky place it inside a box. Take care that the glass slide will be hot after glow discharge.

Note: It is imperative that as soon as the chamber is de-pressurised, the glass surface could become hydrophobic again. A maximum of ten minutes is allowed between the oxygen plasma cleaning and droplet dispensing.

6.2. Cleaning procedure for AFM tip

The surface of the AFM tip needs to have an appropriate surface energy to dispense droplets on glass. It was found that a freshly prepared silicon cantilever tips could not dispense droplets even if the droplet was present on the cantilever. The presence of cantilever is confirmed by doing a dynamic analysis before and after contacting the glycerol droplet. It was found that the peak frequency shifted towards the lower end indicating the presence of a liquid. Figure 6.1 shows the cantilever response before and after contacting a glycerol droplet for a freshly prepared slicon cantilever. Figure 6.1 (c) shows the cantilever response after touching the glow discharged glass slide. It shows the peak at the same location as before. This indicates that the droplet did not flow into the glass slide.

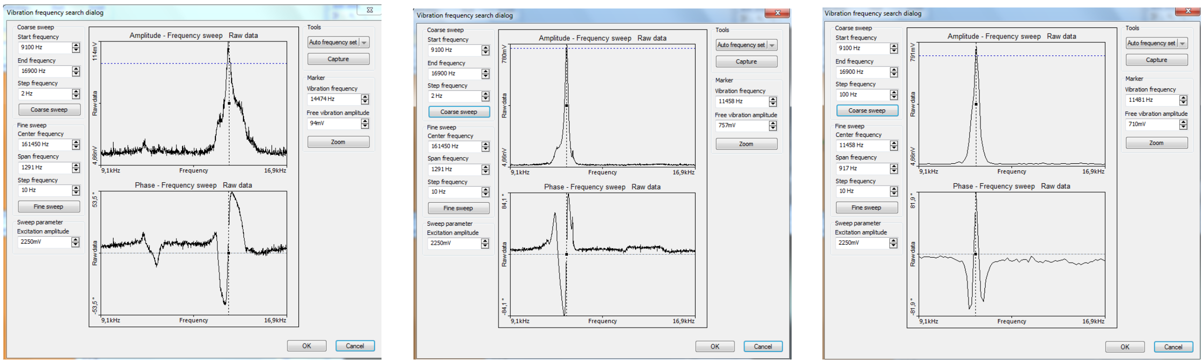
Vibration frequency search dialog
Coarse sweep
Start frequency 9100 Hz
End frequency 16900 Hz
Step frequency 2 Hz
Fine sweep
Center frequency 161450 Hz
Span frequency 1291 Hz
Step frequency 10 Hz
Sweep parameter
Excitation amplitude 2250mV
Tools
Auto frequency set
Marker
Vibration frequency 14474 Hz
Free vibration amplitude 94mV

Vibration frequency search dialog
Coarse sweep
Start frequency 9100 Hz
End frequency 16900 Hz
Step frequency 2 Hz
Fine sweep
Center frequency 161450 Hz
Span frequency 1291 Hz
Step frequency 10 Hz
Sweep parameter
Excitation amplitude 2250mV
Tools
Auto frequency set
Marker
Vibration frequency 11458 Hz
Free vibration amplitude 757mV

Vibration frequency search dialog
Coarse sweep
Start frequency 9100 Hz
End frequency 16900 Hz
Step frequency 100 Hz
Fine sweep
Center frequency 11458 Hz
Span frequency 917 Hz
Step frequency 10 Hz
Sweep parameter
Excitation amplitude 2250mV
Tools
Auto frequency set
Marker
Vibration frequency 11481 Hz
Free vibration amplitude 710mV

a b c

Figure 6.1: The dynamic response of the AFM cantilever (a) before contact with glycerol droplet and (b) after contact with glycerol droplet

Thus the AFM tip needs to be coated with gold to make the surface less hydrophilic. Before coating, the AFM tip needs to be cleaned and Table 6.2 explains the procedure to clean the AFM tip.

Table 6.2: Steps to follow to perform cleaning of AFM tip

	Remove the AFM tip from the AFM instrument using the proper procedure

	Hold the AFM cantilever with the help of a tweezer firmly by its side
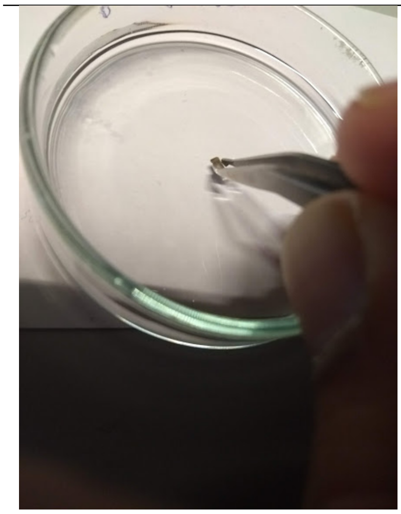	Dip the cantilever inside a petri dish containing DI water. Rinse near the surface for 2 minutes. Remove and dip in another petri dish containing IPA.
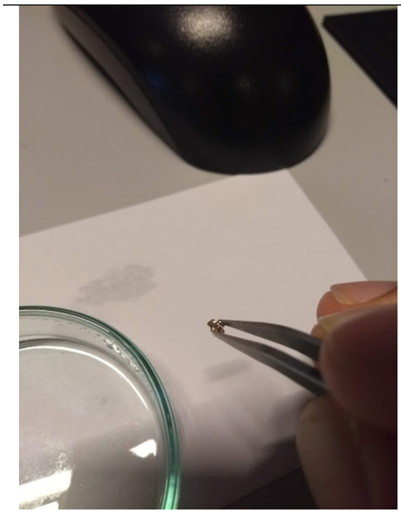	Remove from the petri dish after two minutes and let it dry in air for ten minutes.

Table 6.2: Steps to follow to perform cleaning of AFM tip

Note: Place the AFM tip on a Plasma treatment chamber. Parameters are: 99% (max) power, and time 8 minutes. First place the glass slide for plasma treatment for 15 minutes. Then place the AFM cantilever inside for another 8 minutes.

6.3. Steps to build Mach-Zehnder interferometer

These are the components required before building the setup as listed in Figure 6.2.

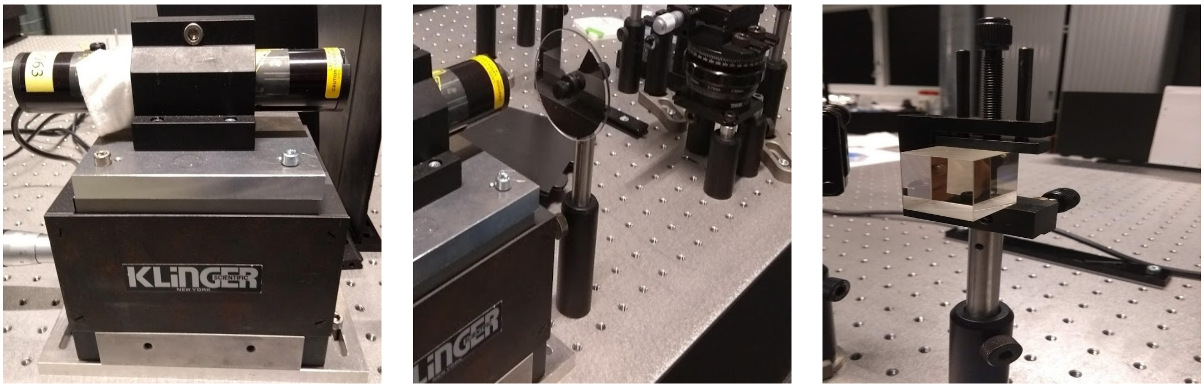

Laser power source with mount Neutral Density Filter Non polarised beam splitter with mount

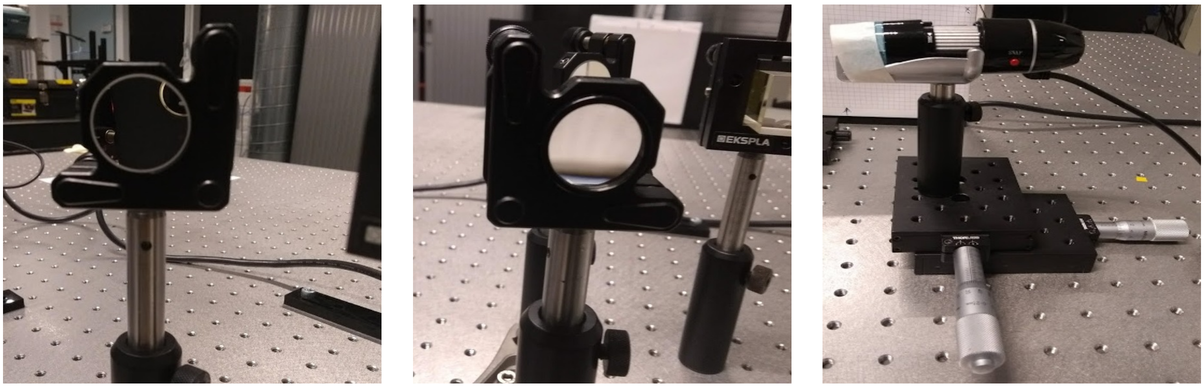

Mirrors Lens CCD camera mounted on linear stage

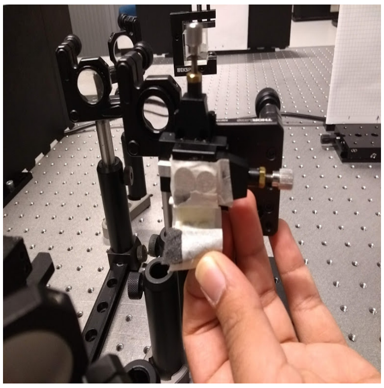

Sample holder with XY stage

Figure 6.2: Components needed to build Mach-Zehnder Interferometer

Follow the steps mentioned in the Table 6.3.

Table 6.3: Steps to follow to build Mach-Zehnder interferometer

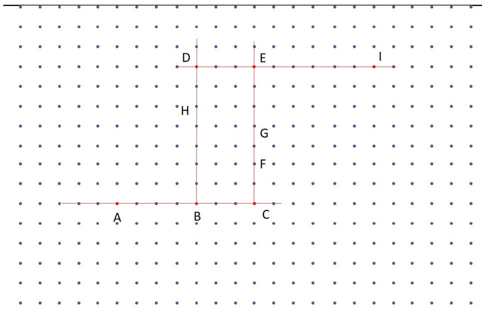	Clear the optical table and define points A to I as shown in the figure
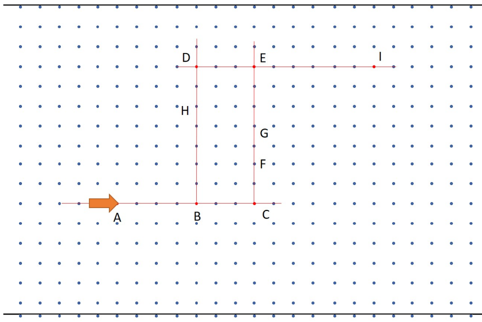	Mount the laser at A with the beam aligned along the line A-B-C
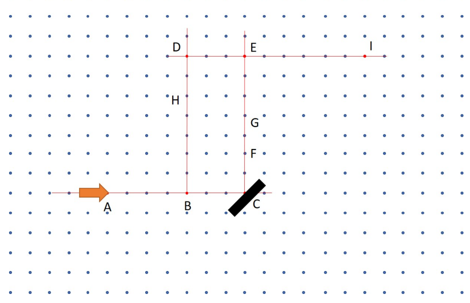	Mount a mirror near C and rotate the angle to 45 degrees such that the test arm now follows the line C-E
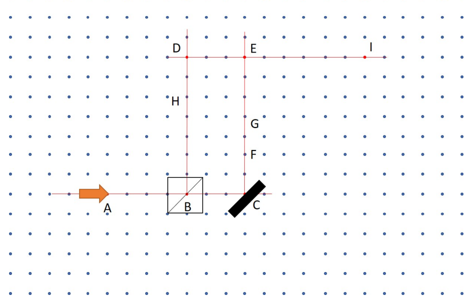	Mount the first beam splitter at B and align the reference arm is aligned with the line B-D
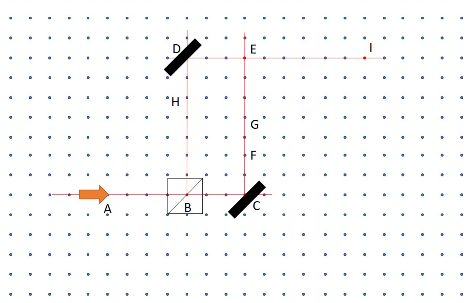	Mount a second mirror near D and rotate the angle to 45 degrees such that the secondary optic axis now follows D-E-I

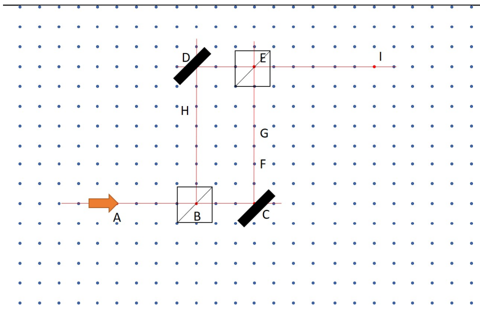

Mount the second beam splitter at E and align so that the reflected light from C-E follows the line E-I

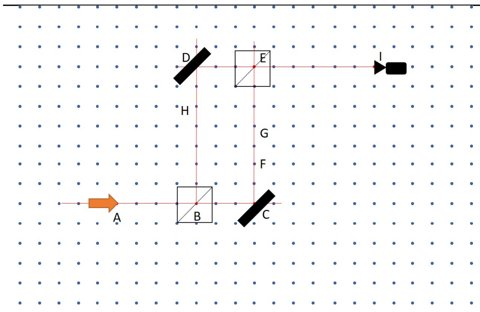

Mount the camera at I and obtain the fringe pattern. If the alignment is correct then the CCD must occupy one full fringe

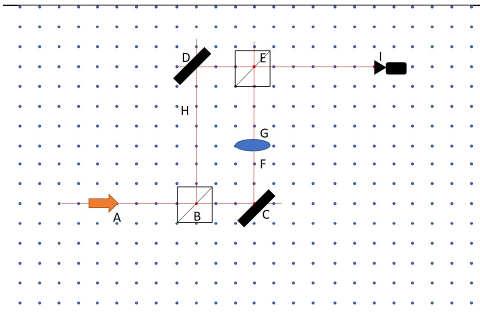

Mount the imaging lens at G

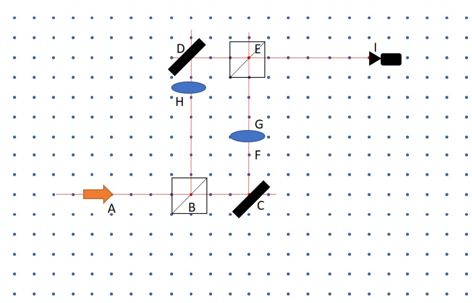

Mount the lens for wavefront corrector near H. Move the lens along B-D until the camera sees either a dark ring or a bright ring. This indicates the interferometer is well aligned. Now introduce misalignment by rotating second beam splitter at E and merging the two laser spots using the lens near H. A set of parallel lines must be visible and the CCD should be uniformly illuminated if the reference arm or test arm is blocked

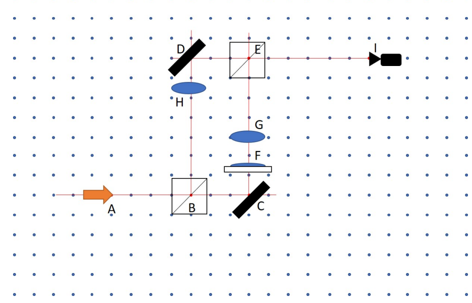

Mount the sample holder with the XY stage near F on a linear stage. Move the linear stage until the surface of the glass is imaged on the CCD

6.4. Matlab Codes

SFFT

```
function Phase = SFFT(I1 , sigma)

    [M N] = size(I1);
    %Filter the zero frequency term
    I1_noMean = I1-mean(mean(I1));
    %Filter the noise present in the data
    I1_filtered = imgaussfilt(I1_noMean,2);
    %Find the fourier transform and use fftshift to center the image
    FT = Fn.ft(I1_filtered);

    %Find the first side peak location
    [peak,loc] = max(abs(FT(:)));
    [y,x] = ind2sub(size(FT),loc);
    pos = [x,y];
    xShift = (320-pos(1));
    yShift = (240-pos(2));

    %Use a Low Pass Filter to filter the side peak
    Filter = getLPFilter(pos,size(I1),sigma);
    newFT = Filter .* FT;
    %Translate the side peak to the center of the image
    C = Fn.ift(imtranslate(newFT,[xShift , yShift]));
    %Find the phase using the complex identity
    Phase = atan(imag(C)./real(C));
end
```

Phase Unwrapping

```

function [unwrappedPhase] = getUnwrappedPhase(I1 ,IBG1);

Phase = SFFT(I1 ,60);
PhaseBG = SFFT(IBG1,60);
sigma = 0.05;
LP = 12;

%To use Volkov Phase Unwrapping algorithm uncomment the next three lines
[unwrapped,approx,K] = phunwrap.unwrapDet(Phase , noiseSigma , LP);
[unwrappedBG,approxBG,KBG] = phunwrap.unwrapDet(PhaseBG, noiseSigma , LP);
unwrappedPhase = approx-approxBG;

%To use 2 pi step method uncomment the next four lines
% unwrapped = unwrap(unwrap(Phase*2 ,[] ,2) ,[] ,1)/2;
% unwrappedBG = unwrap(unwrap(PhaseBG*2 ,[] ,2) ,[] ,1)/2;
% unwrappedPhase = unwrapped - unwrappedBG;
% unwrappedPhase = imgaussfilt(unwrappedPhase,HP);
end
```

Simulated Analysis

```
% Simulation analysis

clear workspace
clear all
clc
```

```

Lambda = 633e-9;                %Input wavelength of laser in m
n = 1.474;                      %Refractive index of droplet
imSize = [1500e-6, 2000e-6];    %Size of the CCD (height x width) in m
pxSize = 3.125e-6;              %Pixel size of CCD in m
Mag = 10;                       %Magnification
CCD = ceil(imSize*M/pxSize);    %Resolution of CCD (height x width)
tilt = [0.1,0.1];               %Use tilt in the system in terms of radians (tilt in Y, tilt in X)
rho = 1250; %kg/m^3             %Density of droplet
r = 60e-6;                      %Radius of droplet

%Find the true phase field for dropelt and without droplet (including tilt)
[Phi1,Phi_ref] = getTruePhase(Lambda,imSize/Mag,CCD,h,n,r,tilt,0);
PhiBG = getTruePhase(Lambda,imSize/Mag,CCD,0,n,r,tilt);

%Add a gaussian noise amplitude (in radian) to the true phase field
noiseSigma = 0.7;
Phi1 = Phi1 + noiseSigma*randn(CCD);
PhiBG = PhiBG + noiseSigma*randn(CCD);

%Obtain the interference pattern using a typical values for dc component
%and modulation amplitude
A = 160;
B = 80;
I1 = A+B*cos(Phi1);
IBG1 = A+B*cos(PhiBG);

%Get the unwrapped phase
unwrapped = getUnwrappedPhase(I1,IBG1);
unwrapped = unwrapped - min(unwrapped(:));

%Convert phase profile into height
height = unwrapped * Lambda /(2*pi*(n-1));
Refheight = Phi_ref * Lambda / (2*pi*(n-1));

diff = height - Refheight;
massUnwrapped = rho * getVol(height);
massTrue = rho * getVol(Refheight);

xlimits = linspace(1,CCD(2)*pxSize,CCD(2))/Mag;
ylimits = linspace(1,CCD(1)*pxSize,CCD(1))/Mag;
surf(xlimits,ylimits,height*1e9); shading interp; colorbar
set(gca,'fontsize',18);
```

6.4.1. Misc codes

```
% Function to output interference phase given parameters of the interferometer
% Input
% Lambda = Wavelength (in m);
% imSize = (1x2) array [height of image (in m) X width of image (in m);
% CCD = (1x2) array [number of pixels in y and x direction];
% h = height of water droplet (in m); n = refractive index;
% r = contact radius of spherical droplet; tilt = (1x2) [tilt in Y and X in
% radian]

function [output,referencePhase] = getTruePhase(Lambda,imSize,CCD,h,n,r,tilt,const)
```

```matlab

    cols = CCD(2); rows = CCD(1);
    imWidth = imSize(2); imHeight = imSize(1);
    tiltX = tilt(2); tiltY = tilt(1);
    % Get optical path length (OPL) in the reference path ignoring

    for i = [1:rows]
        for j = [1:cols]
            OPL_ref(i,j) = (tiltX*(j-1)*imWidth/cols)+(tiltY*(i-1)*imHeight/rows);
        end
    end

    % Calculate OPL in Test Beam

    %Get height profile of water
    if h > 0
        h_water = sphericalCap(r,h,imSize,CCD,const);
    else
        h_water = zeros(rows,cols);
    end

    n_water(1:rows,1:cols) = n;
    OPL_test = (n_water-1).*(h_water);

    OPD = OPL_test - OPL_ref;
    k = 2*pi/Lambda;

    % Calculate deltaPhi using OPD and the fraction of pi

    delPhi = k*OPD;
    referencePhase = k*OPL_test;
    output = abs(delPhi);
end
```

```matlab
function output = sphericalCap(r,h,imSize,CCD,d)
% Function to output a rectangular array, with a spherical cap region in
% it's center. Inputs are:
% r = contact radius of spherical cap; h = height of spherical cap;
% imSize = (1x2) array, [image height (in m) x image width (in m)]
% CCD = (1x2) array, [number of pixels in height x width]

    cols = CCD(2); rows = CCD(1);
    imWidth = imSize(2); imHeight = imSize(1);

    output = zeros(rows,cols);
    theta = 2*atan(h/r);
    R = h/(1-cos(theta));
    xc = round(cols/2);
    yc = round(rows/2);
    zc = h-R;

    for i = 1:rows
        for j = 1:cols
            if ((i-yc)*(imHeight/rows))^2+((j-xc)*(imWidth/cols))^2 <= r^2
            output(i,j) = d + ( zc + ((sqrt(R^2-((j-xc)*imWidth/cols)^2-((i-yc)*
                imHeight/rows)^2))));
```

```
            end
        end
    end

 end
```

```
function output = getLPFilter(pos,imSize,sigma)
            %Get a rectangular low pass filter at a given position for a 2D image
            %and a known sigma
            x = pos(1); y = pos(2);
            imWidth = imSize(1); imHeight = imSize(2);
            output = zeros(imWidth,imHeight);

            %To use a gaussian filter uncommmment the next three lines
            temp = fspecial('gaussian',2*sigma,sigma/4);
            temp = Fn.normalise(temp);
            output(y-sigma:y+sigma-1,x-sigma:x+sigma-1) = temp;

            %To use the disk type filter uncomment the next three lines
%            temp = fspecial('disk',sigma);
%            temp = Fn.normalise(temp);
%            output(y-sigma:y+sigma,x-sigma:x+sigma) = temp;
end
```

```
function Vol = getVol(height)
% Given a 3D height profile return the volume in m^3

    %First find the max z value at the edges and let every number below
    %this be equal to zero
    zlim = max([max(height(1,1:end)),max(height(end-1,1:end)),max(height(1:end,1)),
        max(height(1:end,end-1))]);
    height(height<zlim) = 0;
    summation = sum(height(:));

    %Volume = sum * (pixelSize^2) / (Mag^2)

    Vol = summation * (3.125e-6)^2 / 100;
end
```

```
% Miscellanous functions
classdef Fn
    methods(Static)
        % Function to return fft2 and ifft2 after shifting to center

        %input x = 2D matrix
        function y = ft(x)
        y = fftshift(fft2(fftshift(x)));
        end

        function y1  = ift(x)
        y1 = ifftshift(ifft2(ifftshift(x)));
        end


    end
end
```

Bibliography

[1] B. Topinka, “Hydrophobicity: Will the Drop Stop or Roll?.”

[2] V. Srinivasan, V. K. Pamula, and R. B. Fair, “An integrated digital microfluidic lab-on-a-chip for clinical diagnostics on human physiological fluids,” *Lab Chip*, vol. 4, pp. 310–315, July 2004.

[3] T. Sekitani, Y. Noguchi, U. Zschieschang, H. Klauk, and T. Someya, “Organic transistors manufactured using inkjet technology with subfemtoliter accuracy,” *PNAS*, vol. 105, pp. 4976–4980, Apr. 2008.

[4] J. Jing, J. Reed, J. Huang, X. Hu, V. Clarke, J. Edington, D. Housman, T. S. Anantharaman, E. J. Huff, B. Mishra, B. Porter, A. Shenker, E. Wolfson, C. Hiort, R. Kantor, C. Aston, and D. C. Schwartz, “Automated high resolution optical mapping using arrayed, fluid-fixed DNA molecules,” *PNAS*, vol. 95, pp. 8046–8051, July 1998.

[5] S. A. Arnold, S. Albiez, A. Bieri, A. Syntychaki, R. Adaixo, R. A. McLeod, K. N. Goldie, H. Stahlberg, and T. Braun, “Blotting-free and lossless cryo-electron microscopy grid preparation from nanoliter-sized protein samples and single-cell extracts,” *Journal of Structural Biology*, vol. 197, pp. 220–226, Mar. 2017.

[6] T. Jain, P. Sheehan, J. Crum, B. Carragher, and C. S. Potter, “Spotiton: A prototype for an integrated inkjet dispense and vitrification system for cryo-TEM,” *Journal of Structural Biology*, vol. 179, pp. 68–75, July 2012.

[7] X. Cao, R. d. Gruiter, R. van Oorschot, S. Baldi, H. HosseinNia, and M. K. Ghatkesar, “A model for controlled dosing of femto-litre volume liquids using hollow microcantilever,” *IFAC-PapersOnLine*, vol. 50, pp. 15542–15547, July 2017.

[8] “Reference Finder Grids, for Transmission Electron Microscopy.”

[9] “C-Flat Holey Carbon and Gold Grids for Cryo-TEM.”

[10] C. J. Russo and L. A. Passmore, “Progress towards an optimal specimen support for electron cryomicroscopy,” *Current Opinion in Structural Biology*, vol. 37, pp. 81–89, Apr. 2016.

[11] R. Grimm, D. Typke, M. Bärmann, and W. Baumeister, “Determination of the inelastic mean free path in ice by examination of tilted vesicles and automated most probable loss imaging,” *Ultramicroscopy*, vol. 63, pp. 169–179, July 1996.

[12] “Glycerol G5516.”

[13] H. Hu and R. G. Larson, “Evaporation of a Sessile Droplet on a Substrate,” *The Journal of Physical Chemistry B*, vol. 106, pp. 1334–1344, Feb. 2002.

[14] S. M. Rowan, M. I. Newton, and G. McHale, “Evaporation of Microdroplets and the Wetting of Solid Surfaces,” *J. Phys. Chem.*, vol. 99, pp. 13268–13271, Aug. 1995.

[15] R. Picknett and R. Bexon, “The evaporation of sessile or pendant drops in still air,” *Journal of Colloid and Interface Science*, vol. 61, pp. 336–350, Sept. 1977.

[16] H.-J. Butt, D. S. Golovko, and E. Bonaccurso, “On the Derivation of Young’s Equation for Sessile Drops: Nonequilibrium Effects Due to Evaporation,” *J. Phys. Chem. B*, vol. 111, pp. 5277–5283, May 2007.

[17] D. S. Golovko, H.-J. Butt, and E. Bonaccurso, “Transition in the Evaporation Kinetics of Water Microdrops on Hydrophilic Surfaces,” *Langmuir*, vol. 25, pp. 75–78, Jan. 2009.

[18] J. Arcamone, E. Dujardin, G. Rius, F. Pérez-Murano, and T. Ondarçuhu, “Evaporation of Femtoliter Sessile Droplets Monitored with Nanomechanical Mass Sensors,” *The Journal of Physical Chemistry B*, vol. 111, pp. 13020–13027, Nov. 2007.

[19] C. M. Mate, M. R. Lorenz, and V. J. Novotny, "Atomic force microscopy of polymeric liquid films," *The Journal of Chemical Physics*, vol. 90, pp. 7550–7555, June 1989.

[20] P. Sun, L. Zhong, C. Luo, W. Niu, and X. Lu, "Visual measurement of the evaporation process of a sessile droplet by dual-channel simultaneous phase-shifting interferometry," *Sci Rep*, vol. 5, July 2015.

[21] M. Takeda, H. Ina, and S. Kobayashi, "Fourier-transform method of fringe-pattern analysis for computer-based topography and interferometry," *J. Opt. Soc. Am., JOSA*, vol. 72, pp. 156–160, Jan. 1982.

[22] L. Huang, X. Lu, J. Li, Y. Zhou, J. Xiong, J. Tian, and L. Zhong, "Dynamic phase measurement based on spatial carrier-frequency phase-shifting method," *Opt. Express, OE*, vol. 24, pp. 13744–13753, June 2016.

[23] "TEL - Thèses en ligne - Droplet-based microfluidics at the femtoliter scale."

[24] n. Rose, "Microdispensing technologies in drug discovery," *Drug Discov. Today*, vol. 4, pp. 411–419, Sept. 1999.

[25] D. J. Hayes, D. B. Wallace, and W. R. Cox, *MicroJet Printing of Solder and Polymers for Multi-Chip Modules and Chip-Scale Packages by.*

[26] J. H. Bruning, D. R. Herriott, J. E. Gallagher, D. P. Rosenfeld, A. D. White, and D. J. Brangaccio, "Digital Wavefront Measuring Interferometer for Testing Optical Surfaces and Lenses," *Appl. Opt., AO*, vol. 13, pp. 2693–2703, Nov. 1974.

[27] O. Y. Kwon, "Multichannel phase-shifted interferometer," *Opt. Lett., OL*, vol. 9, pp. 59–61, Feb. 1984.

[28] T. Ikeda, G. Popescu, R. R. Dasari, and M. S. Feld, "Hilbert phase microscopy for investigating fast dynamics in transparent systems," *Opt. Lett., OL*, vol. 30, pp. 1165–1167, May 2005.

[29] W. W. Macy, "Two-dimensional fringe-pattern analysis," *Appl. Opt., AO*, vol. 22, pp. 3898–3901, Dec. 1983.

[30] S. Byrnes, "tmm: Simulate light propagation in multilayer thin and/or thick films using the fresnel equations and transfer matrix method.."

[31] V. V. Volkov and Y. Zhu, "Deterministic phase unwrapping in the presence of noise," *Opt. Lett., OL*, vol. 28, pp. 2156–2158, Nov. 2003.

[32] "Ulf's Cyber Attic - 2d Phase Unwrapping."